INTERNATIONAL JOURNAL FOR NUMERICAL AND ANALYTICAL METHODS IN GEOMECHANICS
Int. J. Numer. Anal. Meth. Geomech. (2017)
Published online in Wiley Online Library (wileyonlinelibrary.com). DOI: 10.1002/nag.2669

Simulation of liquefaction of unsaturated soil using critical state soil model

Veerayut Komolvilas and Mamoru Kikumoto*,†

Department of Civil Engineering, Yokohama National University, Yokohama, Japan

SUMMARY

Several researchers have reported that the mean effective stress of unsaturated soils having a relatively high degree of saturation gradually decreases under fully undrained cyclic loading conditions, and such soils can be finally liquefied like saturated soils. This paper describes a series of simulations of fully undrained cyclic loading on unsaturated soils, conducted using an elastoplastic model for unsaturated soils. This model is a critical state soil model formulated using effective stress tensor for unsaturated soils, which incorporates the following concepts: (a) the volumetric movement of the state boundary surface containing the critical state line owing to the variation in the degree of saturation; (b) the soil water characteristic curve considering the effects of specific volume and hydraulic hysteresis; and (c) the subloading surface concept for considering the effect of density. Void air is assumed to be an ideal gas obeying Boyle's law. The proposed model is validated through comparisons with past results. The simulation results show that the proposed model properly describes the fully undrained cyclic behavior of unsaturated soils, such as liquefaction, compression, and an increase in the degree of saturation. Finally, the effects of the degree of saturation, void ratio, and confining pressure on the cyclic strength of unsaturated soils are described by the simulation results. The liquefaction resistance of unsaturated soils increases as the degree of saturation and the void ratio decrease, and as the confining pressure increases. Furthermore, the degree of saturation has a greater effect on the liquefaction resistance than the confining pressure and void ratio.

Received 29 July 2016; Revised 20 December 2016; Accepted 20 December 2016

KEY WORDS: unsaturated soils; cyclic loading; liquefaction; elastoplasticity; degree of saturation; void ratio

1. INTRODUCTION

Soils are often subjected to cyclic loading under unsaturated conditions in practical situations, such as the deformation of embankments and reclaimed areas during an earthquake. In Japan, the Sanriku–Minami earthquake triggered a landslide in the town of Tsukidate on May 26, 2003. An artificial fill in this disaster area lost its effective confining stress under cyclic loading although the degree of saturation was around 70% [1]. The landfills along the northeastern shorelines of Tokyo Bay were liquefied because of the Great East Japan Earthquake in 2011, which caused soil subsidence in an area of around 42 km^2 [2]. Thus far, several questions have been raised about the liquefaction potential of unsaturated soils.

Recently, many researchers have investigated the cyclic behavior of unsaturated soils by conducting laboratory tests under fully undrained cyclic loading conditions. Ishihara *et al*. [3] studied the effects of the relative density and degree of saturation on the undrained behavior of nearly saturated sand through multiple series of monotonic and cyclic triaxial tests. Selim and Burak [4] conducted a torsional shear test on unsaturated silty clay to explore the small and large strain behavior of unsaturated soils. Okamura and Noguchi [5] observed the influence of air and suction pressure on the liquefaction

*Correspondence to: M. Kikumoto, Department of Civil Engineering, Yokohama National University, Yokohama, Japan.
†E-mail: kikumoto@ynu.ac.jp

resistance of unsaturated soils through a series of cyclic triaxial tests on a fine, clean sand and a non-plastic silt under fully undrained conditions. Liu and Xu [6] studied the effects of the degree of saturation, relative density, and confining pressure on the cyclic behavior of saturated and unsaturated sand by conducting a series of strain-controlled cyclic triaxial tests under fully undrained conditions. Tsukamoto *et al*. [7] conducted a series of undrained stress-controlled cyclic triaxial tests on unsaturated sand to examine the changes in the cyclic resistance of silty sand with different grain compositions. Further, Unno *et al*. [1, 8, 9] conducted a series of strain-controlled cyclic triaxial tests on unsaturated soils under fully undrained conditions to study the liquefaction behavior of such soils. Importantly, the existing experimental studies have revealed that the mean effective stress of an unsaturated soil having a relatively high degree of saturation gradually decreases and such a soil can be finally liquefied in a manner similar to saturated soils.

So as to predict the behavior of unsaturated soils, the coupling of mechanical and hydraulic behaviors needs to be considered. Over the past decade, many researchers have proposed the coupling of an elastoplastic constitutive model and a water retention curve model to capture the behavior of unsaturated soils. Khalili *et al*. [10] proposed coupled flow and deformation models based on the effective stress concept for cyclic analysis using the bounding surface plasticity, the hydraulic hysteresis considering the change in density, and the coupled effect of suction hardening. Yang *et al*. [11] developed a constitutive model for unsaturated cemented soils under cyclic loading using the bond damage theory for considering cemented soils, the Barcelona Basic Model for describing the effect of suction on cohesion, and the bounding surface plasticity concept for modeling the strain due to cyclic loading. Kikumoto *et al*. [12] proposed a simple critical state model for unsaturated soils considering the degree of saturation-induced hardening and the effects of hydraulic hysteresis and density on the water retention curve, which is capable of describing collapse and compaction behaviors. Liu and Muraleetharan [13, 14] proposed a coupled hydro-mechanical constitutive model in the general stress space for unsaturated sands and silts. They considered the hysteretic properties of the soil–water characteristic curve (SWCC) using the bounding surface plasticity concept. In addition, they investigated the effect of suction on hardening through the irrecoverable water content calculated using the SWCC model. However, thus far, the liquefaction of unsaturated soils has not been simulated using the aforementioned models. Meanwhile, Unno *et al*. [9] proposed a simplified elastoplastic constitutive model combined with the three-phase porous media theory and the modified SWCC model to study the effect of pore air pressure on the cyclic behavior of unsaturated sandy soils; however, the suction does not affect the yield surface of unsaturated soils in this model.

The main objectives of this paper are as follows: (i) to extend the simple elastoplastic model proposed by Kikumoto *et al*. [12] to three-dimensional problems to predict the liquefaction behavior of unsaturated soils; (2) to present a series of simulations of fully undrained cyclic loading on unsaturated soils using the aforementioned model; and (3) to propose a standard for the liquefaction resistance of unsaturated soils in relation to the degree of saturation, specific volume, and effective confining pressure. This model is a critical state soil model formulated using effective stress tensor for unsaturated soils, which incorporates the following concepts: the volumetric movement of the state boundary surface containing the critical state line (CSL) and normal consolidation line (NCL) owing to the variation in the degree of saturation; the SWCC model considering the effects of specific volume and hydraulic hysteresis; and the subloading surface concept [15]. The volumetric behavior of void air is described by Boyle's law. The validity of the proposed model is verified via comparisons with experimental results [9]. The simulations show that the proposed model properly describes the fully undrained cyclic behavior of unsaturated soils, such as liquefaction, compression, and increase in the degree of saturation. Finally, the effects of the degree of saturation, void ratio, and confining pressure on the cyclic strength of unsaturated soils are studied through the simulations, and three-dimensional surfaces of the liquefaction resistance of unsaturated soils are presented.

2. BASIC CONCEPTS

The basic concepts applied to formulate a model for unsaturated soils are described herein. As for the notations and symbols, bold letters denote vectors and matrices; '·' denotes an inner product of two

DOI: 10.1002/nag

vectors (e.g., $\mathbf{a}\cdot\mathbf{b}=a_i b_i$) or a single contraction of adjacent indices of two tensors (e.g., $(\mathbf{c}\cdot\mathbf{d})_{ij}=c_{ik}d_{kj}$); ':' denotes an inner product of two second-order tensors (e.g., $\mathbf{c}:\mathbf{d}=c_{ij}d_{ij}$) or a double contraction of adjacent indices of tensors of rank two and higher (e.g., $(\mathbf{e}:\mathbf{c})_{ij}=e_{ijkl}c_{kl}$); $\otimes$ denotes a tensor product of two vectors (e.g., $(\mathbf{a}\otimes\mathbf{b})_{ij}=a_i b_j$) or a tensor product of two second-order tensors (e.g., $(\mathbf{c}\otimes\mathbf{d})_{ijkl}=a_{ij}b_{kl}$); '‖‖' denotes the norm of a first-order tensor (e.g., $\|\mathbf{a}\|=\sqrt{\mathbf{a}:\mathbf{a}}=\sqrt{a_i a_i}$) or a second-order tensor (e.g., $\|\mathbf{c}\|=\sqrt{\mathbf{c}:\mathbf{c}}=\sqrt{c_{ij}c_{ij}}$); $\mathbf{1}$ is the second-order identity tensor; $\boldsymbol{I}$ is the fourth-order identity tensor $\left(I_{ijkl}=\frac{1}{2}\left(\delta_{ik}\delta_{jl}+\delta_{il}\delta_{jk}\right)\right)$; '' denotes the time derivative; and the subscript zero denotes the initial state (e.g., v_0 = initial specific volume).

2.1. Effective stress

Sivakumar [16] indicated that the critical state stress ratio is uniquely defined by Bishop's mean effective stress versus the deviator stress plane regardless of the degree of saturation. Hence, a unique critical state friction angle can be assumed in a model for unsaturated soils if it is formulated on the basis of Bishop's effective stress tensor [17]. Thus, we formulate the model for unsaturated soils on the basis of Bishop's effective stress tensor $\boldsymbol{\sigma}''$, defined by:

$$\boldsymbol{\sigma}'' = \boldsymbol{\sigma} - (1-\chi)u_a\mathbf{1} - \chi u_w\mathbf{1} = (\boldsymbol{\sigma} - u_a\mathbf{1}) + \chi(u_a - u_w)\mathbf{1} = \boldsymbol{\sigma}_{\mathbf{net}} + \chi s\mathbf{1} \tag{1}$$

where $\boldsymbol{\sigma}$, $\boldsymbol{\sigma}_{\mathbf{net}}$, u_a, u_w, and s represent Cauchy's total stress tensor, Cauchy's net stress tensor, air pressure, water pressure, and suction, respectively. Further, χ is an effective stress parameter given by a monotonic increasing function of the degree of saturation S_r ranging from 0 for dry conditions to 1 for fully saturated conditions; for simplicity, it is assumed to be equal to S_r in this study.

$$\boldsymbol{\sigma}'' = \boldsymbol{\sigma} - (1-S_r)u_a\mathbf{1} - S_r u_w\mathbf{1} = \boldsymbol{\sigma}_{net} + S_r s\mathbf{1} \tag{2}$$

Equation (2) has been first proposed by Schrefler [18] in a similar expression as Bishop's effective stress, but using the degree of saturation S_r instead of χ. Borja [19] has also derived Equation (2) by using the principles of thermodynamics.

2.2. Soil water characteristic curve considering the effects of density and hydraulic hysteresis

Considering the possible range of the degree of saturation S_r, the effective degree of saturation S_e is given by

$$\frac{S_r - S_{min}}{S_{max} - S_{min}} = S_e \tag{3}$$

where S_{max} and S_{min} are the maximum and minimum degrees of saturation, respectively. Classical SWCC models give the effective degree of saturation S_e as a monotonic decreasing, single-valued function of suction s ranging from 0 to 1 (e.g., Gardner [20]; Brooks and Corey [21]; Fredlund and Xing [22]; van Genuchten [23]). Any of such classical models can be applied to the proposed SWCC model presented here. For this study, we selected the following function proposed by van Genuchten [23].

$$S_e = S_e(s) = \{1 + (\alpha s)^n\}^{-m} \tag{4}$$

where α, n, and m are material parameters.

However, past experimental studies (e.g., Tarantino and Tombolato [24]) indicate that volumetric behavior influences the SWCC and that denser soils tend to retain a higher S_r. Therefore, we extended classical SWCC models that assume a unique relationship between suction and degree of saturation using a modified suction s^*, where the effect of density is incorporated as

$$s^* = s\left(\frac{e}{e_{ref}}\right)^{\xi_e} \tag{5}$$

where e is the void ratio, e_{ref} is a reference void ratio for which we use the void ratio of saturated, normally consolidated soils under atmospheric pressure p_a (= 98 kPa), and ξ_e is a parameter controlling the effect of density. Thus, using s^*, we can rewrite Equation (4) as

DOI: 10.1002/nag

$$S_e = S_e(s^*) = \{1 + (\alpha s^*)^n\}^{-m} \tag{6}$$

Further, it is well known that SWCCs trace hysteretic paths according to drying and wetting histories [25–27]. Therefore, we define the main drying and wetting curves by Equation (6) as the highest and lowest boundaries of the degree of saturation, S_r^d and S_r^w, as follows:

$$\frac{S_r^A - S_{min}}{S_{max} - S_{min}} = S_e^A(s^*) = \left\{1 + \left(\alpha^A s^*\right)^n\right\}^{-m}, \quad A = d, w \tag{7}$$

where d and w denote the main drying and wetting curves, respectively. The main drying and wetting paths are schematically illustrated in Figure 1. We need to set different values for the parameters α^d and α^w for the main drying and wetting curves, respectively, whereas we use the same values for the other parameters, namely, n and m. As S_r^d is always larger than S_r^w at the same suction value, α^d should be set to a smaller value than α^w.

So as to define the current state (s^*, S_r), we use a ratio I_h of interior division of the current state between two reference states on the main curves under the same modified suction as follows:

$$I_h = \frac{S_r - S_r^w}{S_r^d - S_r^w}. \tag{8}$$

As the current state (s^*, S_r) is always located between the two main curves, I_h always takes a value between 0 and 1. Further, I_h can be used as a key state variable that reflects the wetting and drying histories. It increases monotonically to 1 with decreasing S_r (drying) as the current state approaches the main drying curve, and it decreases monotonically to 0 with increasing S_r (wetting) as the current state approaches the main wetting curve. Thus, an evolution law for I_h must satisfy the following requirements:

$$\dot{I}_h \begin{cases} \geq 0 & \text{when} \quad \dot{S}_r \leq 0 \\ \leq 0 & \text{when} \quad \dot{S}_r \geq 0 \\ = 0 & \text{when} \quad I_h = 0 \text{ or } I_h = 1 \end{cases}. \tag{9}$$

An evolution law given by the following equation satisfies this requirement and is employed in the present study:

$$\dot{I}_h = \frac{dI_h}{dS_r}\dot{S}_r \quad \text{where} \quad \frac{dI_h}{dS_r} = \begin{cases} -\xi_h(1 - I_h)^3 & \text{when} \quad \dot{S}_r \leq 0 \\ -\xi_h {I_h}^3 & \text{when} \quad \dot{S}_r > 0 \end{cases} \tag{10}$$

where ξ_h is a material constant controlling the effect of suction histories.

From Equations (5), (7), and (8), the time derivative of the degree of saturation is given by increments of suction s, void ratio e, and variable I_h as

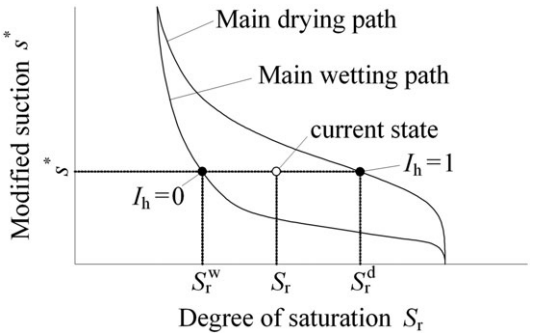

Figure 1. Modeling of hysteresis in water retention curve [12].

DOI: 10.1002/nag

$$\dot{S}_{\mathrm{r}} = \frac{\partial S_{\mathrm{r}}}{\partial s}\dot{s} + \frac{\partial S_{\mathrm{r}}}{\partial e}\dot{e} + \frac{\partial S_{\mathrm{r}}}{\partial I_{\mathrm{h}}}\dot{I}_{\mathrm{h}}. \tag{11}$$

Substituting Equation (10), we finally obtain

$$\dot{S}_r = \frac{\frac{\partial S_{\mathrm{r}}}{\partial s}\dot{s} + \frac{\partial S_{\mathrm{r}}}{\partial e}\dot{e}}{1 - \frac{\partial S_{\mathrm{r}}}{\partial I_{\mathrm{h}}}\frac{\mathrm{d}I_{\mathrm{h}}}{\mathrm{d}S_{\mathrm{r}}}}. \tag{12}$$

2.3. Stress–strain relationship for unsaturated soil

A critical state soil model for unsaturated soils was formulated by Kikumoto *et al*. [12] on the basis of the modified Cam clay model [28], which incorporates the subloading surface concept [15] and the volumetric movement of the state boundary surface (Figure 2) owing to the variation in S_{r}. We extend this model to three-dimensional problems herein. For the model, we first assume additive decomposition of the total strain rate tensor as

$$\dot{\boldsymbol{\varepsilon}} = \dot{\boldsymbol{\varepsilon}}^{\mathrm{e}} + \dot{\boldsymbol{\varepsilon}}^{\mathrm{p}} \tag{13}$$

where $\dot{\boldsymbol{\varepsilon}}^{\mathrm{e}}$ and $\dot{\boldsymbol{\varepsilon}}^{\mathrm{p}}$ are elastic and plastic strain rate tensors, respectively.

(a) Elastic stress–strain relationship

For the elastic stress–strain relationship, we use a conventional, nonlinear elastic bulk modulus for soils, given by

$$K = \frac{v_0}{\kappa}p'' \tag{14}$$

where v_0 is the initial specific volume, κ is the swelling index that represents the slope of the elastic volumetric relationship in the semi-logarithmic ln p''–v plane, and Poisson's ratio v_{e} is assumed to be constant. Thus, the rate form of the elastic relationship is given by

$$\dot{\boldsymbol{\sigma}}'' = \boldsymbol{D}^{\mathrm{e}} : \dot{\boldsymbol{\varepsilon}}^{\mathrm{e}} \tag{15}$$

where $\dot{\boldsymbol{\sigma}}''$ is the rate of effective stress tensor for unsaturated soils and $\boldsymbol{D}^{\mathrm{e}}$ is the elastic stiffness tensor given by

$$\boldsymbol{D}^{\mathrm{e}} = K\mathbf{1}\otimes\mathbf{1} + 2G\left(\boldsymbol{I} - \frac{1}{3}\mathbf{1}\otimes\mathbf{1}\right) \tag{16}$$

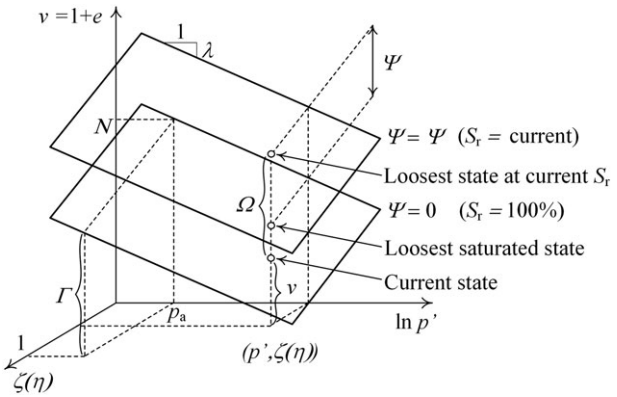

Figure 2. State boundary surface moving with S_{r} and state variable Ω under the effect of packing density.

DOI: 10.1002/nag

where G is the shear modulus given by

$$G = \frac{3K(1-2\nu_e)}{2(1+\nu_e)}. \tag{17}$$

As an inverse tensor of the elastic stiffness tensor $\boldsymbol{D}^e$ always exists, we obtain

$$\dot{\boldsymbol{\varepsilon}}^e = \boldsymbol{D}^{e-1} : \dot{\boldsymbol{\sigma}}'' \tag{18}$$

(b) Yield function for unsaturated soil based on subloading surface concept

The specific volume v_{sbs}^{sat} of a saturated soil on the state boundary surface that defines the loosest state (maximum specific volume) of the saturated soil for the given mean effective stress p' and deviator stress q can be expressed as

$$v_{sbs}^{sat} = N - \lambda \ln \frac{p'}{p_a} + (\Gamma - N)\zeta(\eta) \tag{19}$$

where p' is the mean effective stress $\frac{\mathrm{tr}\boldsymbol{\sigma}'}{3}$, η is the stress ratio q/p', $q\left(=\sqrt{\frac{3}{2}\boldsymbol{s}:\boldsymbol{s}}=\sqrt{\frac{3}{2}\left\{\boldsymbol{\sigma}:\boldsymbol{\sigma}-\frac{1}{3}(\mathrm{tr}\boldsymbol{\sigma})^2\right\}}\right)$ is the deviator stress, and $\boldsymbol{s}(=\boldsymbol{\sigma}-p\boldsymbol{1})$ is the deviator stress tensor. Further, N and Γ are the reference specific volumes of saturated, normally consolidated soil under atmospheric pressure p_a in the isotropic stress state (η = 0) and critical state (η = M), respectively, λ is the compression index, and $\zeta(\eta)$ is a monotonic increasing function of η that satisfies 0 on the NCL with η = 0 and 1 on the CSL with η = M. We employ the following function based on the modified Cam clay model:

$$\zeta(\eta) = \frac{\ln\left\{1+\left(\frac{\eta}{M}\right)^2\right\}}{\ln 2} \tag{20}$$

where M is the stress ratio in the critical state.

As an unsaturated soil exhibits a relatively high stiffness and tends to retain a larger specific volume than a saturated soil, the state boundary surface is assumed to shift upward (downward) as the degree of saturation S_r decreases (increases) in the direction of the specific volume axis. Thus, using a new variable $\Psi(S_r)$ to represent the upward shift of the state boundary surface in the v direction, we define the specific volume v_{sbs}^{unsat} on the state boundary surface of the unsaturated soil using mean effective stress p'' in a manner similar to Equation (19) as

$$v_{sbs}^{unsat} = N - \lambda \ln \frac{p''}{p_a} + (\Gamma - N)\zeta(\eta) + \Psi \tag{21}$$

where Ψ is assumed to be a monotonic decreasing function of the degree of saturation S_r, which always takes a non-negative value and is equal to 0 under the fully saturated condition (S_r = 1). Thus, we introduce a simple linear relationship for Ψ as

$$\Psi = \psi(1 - S_r) \tag{22}$$

where ψ is a material parameter representing the volumetric distance of the state boundary surface for dried and saturated states in the specific volume direction.

So as to consider the effect of specific volume, the subloading surface concept [15] is applied to our model. According to this concept, soil exhibits elastoplastic, irreversible deformation even below the state boundary surface and then gradually approaches the state boundary surface with loading. Therefore, the cyclic behavior of unsaturated soils can therefore be predicted relatively well using this concept. On the other hand, classical models without the subloading surface concept will predict purely elastic behavior within the yield surface and cannot simulate the cyclic behavior of soil. Taking a state variable Ω as the difference between the specific volume of the current state and that

DOI: 10.1002/nag

on the state boundary surface under the same stress (p', η), we can represent an arbitrary specific volume v of an unsaturated soil using Ω as

$$v = v_{\mathrm{sbs}}^{\mathrm{unsat}} - \Omega = N - \lambda \ln \frac{p''}{p_{\mathrm{a}}} + (\Gamma - N)\zeta(\eta) + \Psi(S_{\mathrm{r}}) - \Omega. \tag{23}$$

The definition of the state variable $\Omega(\geq 0)$ is shown in Figure 2. Although Been and Jefferies [29] proposed a similar state parameter as the volumetric distance of the soil from the reference state on the steady state line under the current mean effective stress, our parameter Ω always refers to the volumetric distance from the current state to the loosest state of the soil (specific volume on the state boundary surface) under the current stress condition (p', q) and the current degree of saturation S_{r}. As Ω necessarily decreases with the development of plastic deformation and finally converges to 0, an evolution law of Ω can be represented by

$$\frac{\dot{\Omega}}{v_0} = -\omega \Omega |\Omega| \left\| \dot{\boldsymbol{\varepsilon}}^{\mathrm{p}} \right\| \tag{24}$$

where ω is a parameter controlling the effect of density.

We can obtain the current specific volume v from Equation (23), and we can obtain the initial specific volume v_0 by substituting the initial states $v = v_0$, $\Psi = \Psi_0$, $\Omega = \Omega_0$, $p'' = p_0''$, and $q = 0$ into Equation (23).

$$v_0 = N - \lambda \ln \frac{p_0''}{p_{\mathrm{a}}} + \Psi_0 - \Omega_0 \tag{25}$$

The total volumetric strain (compression is taken to be positive) generated from the initial state to the current state is given by

$$\varepsilon_{\mathrm{v}} = -\frac{\mathrm{d}v}{v_0} = \frac{v_0 - v}{v_0} \tag{26}$$

By substituting Equations (23) and (25) into (26), we obtain

$$\varepsilon_{\mathrm{v}} = \frac{1}{v_0} \left\{ \lambda \ln \frac{p''}{p_0''} + (N - \Gamma)\zeta(\eta) - (\Psi - \Psi_0) + (\Omega - \Omega_0) \right\}. \tag{27}$$

Taking the trace on both sides of Equation (15), we obtain the elastic volumetric strain as

$$\varepsilon_{\mathrm{v}}^{\mathrm{e}} = \frac{\kappa}{v_0} \ln \frac{p''}{p_0''}. \tag{28}$$

The plastic volumetric strain can be determined by taking the difference between the total volumetric strain and the elastic volumetric strain. From Equations (27) and (28), we obtain

$$\varepsilon_{\mathrm{v}}^{\mathrm{p}} = \frac{1}{v_0} \left\{ (\lambda - \kappa) \ln \frac{p''}{p_0''} + (N - \Gamma)\zeta(\eta) - (\Psi - \Psi_0) + (\Omega - \Omega_0) \right\}. \tag{29}$$

From Equation (29), the yield function f for an unsaturated soil can be written as

$$f = \frac{1}{v_0} \left\{ (\lambda - \kappa) \ln \frac{p''}{p_0''} + (N - \Gamma)\zeta(\eta) - (\Psi - \Psi_0) + (\Omega - \Omega_0) \right\} - \varepsilon_{\mathrm{v}}^{\mathrm{p}}. \tag{30}$$

An associated flow is assumed in the model, and the function f is used as the plastic potential function as

$$\dot{\boldsymbol{\varepsilon}}^{\mathrm{p}} = \langle \dot{\Lambda} \rangle \frac{\partial f}{\partial \boldsymbol{\sigma}''} \tag{31}$$

DOI: 10.1002/nag

where $\dot{\Lambda}$ is the rate of the plastic multiplier and $\langle\ \rangle$ is a Macaulay brackets, which denote the ramp function as $x = \begin{cases} x & \text{if } x > 0 \\ 0 & \text{if } x \leq 0 \end{cases}$.

As the soil exhibits an unlimited distortional strain in the critical state without any change in stress or volume, the derivatives of the yield function $f\left(p'', q, \varepsilon_v^p, \Psi, \Omega\right)$ with respect to p'' becomes 0 when $\eta = M$. Thus, $(\lambda - \kappa)$ is equal to $(N - \Gamma)\ln 2$ when Equation (20) is applied. Equation (30) can be finally rearranged as

$$f = \frac{\lambda - \kappa}{v_0}\left[\ln\frac{p''}{p_0''} + \ln\left\{1 + \left(\frac{\eta}{M}\right)^2\right\}\right] - \frac{\Psi - \Psi_0}{v_0} + \frac{\Omega - \Omega_0}{v_0} - \varepsilon_v^p \tag{32}$$

(c) Elastoplastic stress–strain relationship

Taking the time derivative of the yield function $f\left(\boldsymbol{\sigma}'', \varepsilon_v^p, \Psi, \Omega\right)$ given by Equation (32), we obtain the consistency condition as

$$\dot{f} = \frac{\partial f}{\partial \boldsymbol{\sigma}''} : \dot{\boldsymbol{\sigma}}'' + \frac{\partial f}{\partial \Psi}\dot{\Psi} + \frac{\partial f}{\partial \Omega}\dot{\Omega} + \frac{\partial f}{\partial \varepsilon_v^p}\dot{\varepsilon}_v^p = 0. \tag{33}$$

Substituting Equation (31) and the evolution laws of Ψ and $\boldsymbol{\Omega}$, given by Equations (22) and (24), respectively, into (33), we obtain

$$\frac{\partial f}{\partial \boldsymbol{\sigma}''} : \dot{\boldsymbol{\sigma}}'' + \frac{\psi}{v_0}\dot{S}_r - \omega\Omega|\Omega|\langle\dot{\Lambda}\rangle\left\|\frac{\partial f}{\partial \boldsymbol{\sigma}''}\right\| - \langle\dot{\Lambda}\rangle\frac{\partial f}{\partial p''} = 0. \tag{34}$$

From Equations (13) and (18), the stress rate tensor is given by

$$\dot{\boldsymbol{\sigma}}'' = \boldsymbol{D}^e : \left(\dot{\boldsymbol{\varepsilon}} - \dot{\boldsymbol{\varepsilon}}^p\right) = \boldsymbol{D}^e : \left(\dot{\boldsymbol{\varepsilon}} - \langle\dot{\Lambda}\rangle\frac{\partial f}{\partial \boldsymbol{\sigma}''}\right) \tag{35}$$

We obtain the rate of the plastic multiplier from Equations (34) and (35) as follows:

$$\langle\dot{\Lambda}\rangle = \left\langle \frac{\frac{\partial f}{\partial \boldsymbol{\sigma}''} : \boldsymbol{D}^e : \dot{\boldsymbol{\varepsilon}} + \frac{\psi}{v_0}\dot{S}_r}{\frac{\partial f}{\partial p''} + \omega\Omega|\Omega|\left\|\frac{\partial f}{\partial \boldsymbol{\sigma}''}\right\| + \frac{\partial f}{\partial \boldsymbol{\sigma}''} : \boldsymbol{D}^e : \frac{\partial f}{\partial \boldsymbol{\sigma}''}} \right\rangle \tag{36}$$

Finally, we obtain the rate form of the elastoplastic stress–strain relationship from Equations (13), (18), (31), and (36).

$$\dot{\boldsymbol{\sigma}}'' = \boldsymbol{D}^e : \dot{\boldsymbol{\varepsilon}} - \left\langle \frac{\frac{\partial f}{\partial \boldsymbol{\sigma}''} : \boldsymbol{D}^e : \dot{\boldsymbol{\varepsilon}} + \frac{\psi}{v_0}\dot{S}_r}{\frac{\partial f}{\partial p''} + \omega\Omega|\Omega|\left\|\frac{\partial f}{\partial \boldsymbol{\sigma}''}\right\| + \frac{\partial f}{\partial \boldsymbol{\sigma}''} : \boldsymbol{D}^e : \frac{\partial f}{\partial \boldsymbol{\sigma}''}} \right\rangle \boldsymbol{D}^e : \frac{\partial f}{\partial \boldsymbol{\sigma}''} \tag{37}$$

When the rate of the plastic multiplier $\dot{\Lambda}$ is positive, the rate form of the elastoplastic stress–strain relationship can be expressed as

$$\dot{\boldsymbol{\sigma}}'' = \boldsymbol{D}^{ep} : \dot{\boldsymbol{\varepsilon}} - \boldsymbol{D}^{Sr}\dot{S}_r \tag{38}$$

where $\boldsymbol{D}^{ep}$ and $\boldsymbol{D}^{Sr}$ are defined as follows:

$$\boldsymbol{D}^{ep} = \boldsymbol{D}^e - \frac{\boldsymbol{D}^e : \frac{\partial f}{\partial \boldsymbol{\sigma}''} \otimes \frac{\partial f}{\partial \boldsymbol{\sigma}''} : \boldsymbol{D}^e}{\frac{\partial f}{\partial p''} + \omega\Omega|\Omega|\left\|\frac{\partial f}{\partial \boldsymbol{\sigma}''}\right\| + \frac{\partial f}{\partial \boldsymbol{\sigma}''} : \boldsymbol{D}^e : \frac{\partial f}{\partial \boldsymbol{\sigma}''}} \tag{39}$$

$$\boldsymbol{D}^{Sr} = \frac{\boldsymbol{D}^e : \frac{\partial f}{\partial \boldsymbol{\sigma}''}\frac{\psi}{v_0}}{\frac{\partial f}{\partial p''} + \omega\Omega|\Omega|\left\|\frac{\partial f}{\partial \boldsymbol{\sigma}''}\right\| + \frac{\partial f}{\partial \boldsymbol{\sigma}''} : \boldsymbol{D}^e : \frac{\partial f}{\partial \boldsymbol{\sigma}''}} \tag{40}$$

DOI: 10.1002/nag

2.4. Calibration of model parameters

The parameters of a model for unsaturated soils [12] can be categorized into two types: parameters for the water retention curve and parameters for the stress–strain characteristics.

The model parameters for the water retention curve can be calibrated by fitting the water retention curve. Note that S_{min}, S_{max}, α^w, α^d, n, and m are parameters for the main wetting and drying curves described by the van Genuchten model, and ξ_h and ξ_e are the parameters controlling the effect of suction histories and density, respectively.

There are two sets of model parameters for the stress–strain characteristics. The first set (λ, κ, N, M, and ν_e) can be readily obtained from the results of elementary tests on saturated samples. The results of isotropic consolidation tests on saturated samples plotted in the e–ln p'' plane can be used to determine λ from the slope of the NCL, κ from the slope of the unloading part, and N from the specific volume on the NCL under atmospheric pressure. The slope of the CSL in the q–p'' plane, M, and Poisson's ratio, ν_e, are calibrated from the result of triaxial compression tests. The parameter ψ, which controls the effect of S_r on the position of the state boundary surface, can be determined by the result of soaking tests on dried or unsaturated soil samples or by the results of constant suction compression tests on unsaturated soil samples; however, it is deduced by fitting the simulations of cyclic loading tests under varying degrees of saturation to their corresponding experimental results in this study. The parameter ω, which controls the effect of density, is the only parameter that needs to be calibrated by a trial-and-error procedure to fit the experimental results of the soils at different densities.

3. SIMULATIONS

All the analyses were performed using the parameters of Tsukidate volcanic sand (non-plastic sand), which has a specific gravity of 2.478 [9] (Tables I and II). In the simulation of the cyclic triaxial tests for the calibration of the model parameters and validation of the model, three types of initial shearing states were considered (Table III). Saturated soil was used in case c-1, while unsaturated soils having different degrees of saturation were considered under varying pore air pressure in cases c-2 and c-3. Then, cyclic shearing, for which the axial strain amplitude was increased every 10 cycles as shown in Figure 3, was applied to the specimens under the fully undrained conditions at a constant confining pressure.

3.1. Fully undrained simulation

The fully undrained condition, that is, unexhausted air and undrained water, is the condition where air and water are unable to drain out of the soil. In other words, the mass of water and air are constant. So as to simulate the unexhausted air condition, we assumed that air is an ideal gas, and the temperature is constant. Therefore, Boyle's law, which states that the absolute pressure of a given mass of an ideal gas is inversely proportional to its volume at a constant temperature, can be used as

$$u_a V_a = \text{constant} \tag{41}$$

where u_a is the pore air pressure and V_a is the volume of pore air. As the volume of soil particles, V_s, is constant, we obtain

Table I. Parameters for stress–strain characteristics.

λ	0.123	Compression index
κ	0.022	Swelling index
M	1.5	Stress ratio in critical state
ν_e	0.3	Poisson's ratio
N	1.90	Reference specific volume on the state boundary surfaceunder $p'' = p_a$, $q = 0$, and $S_r = 1$
ω	90.0	Effect of density
ψ	0.90	Effect of S_r on the position of the state boundary surface

DOI: 10.1002/nag

Table II. Parameters for water retention curve.

S_{max}	1.00	
S_{min}	0.20	Parameters for main wetting and drying curves described by van Genuchten's soil–water characteristic curve equation
α^d (1/kPa)	0.04	
α^w (1/kPa)	2.00	
n	1.724	
m	0.42	
ξ_h	10.0	Influence of suction histories
ξ_e	2.5	Influence of void ratio
e_{ref}	0.90	Reference void ratio

Table III. Initial state of cyclic shearing simulation [9].

Case no.	c-1	c-2	c-3
Air pressure u_a (kPa)	—	6.0	14.8
Water pressure u_w (kPa)	0.0	0.0	0.0
Suction s (kPa)	—	6.0	14.8
Mean net stress p_{net} (kPa)	—	18.6	19.9
Mean effective stress p'' (kPa)	20.8	23.3	30.8

Note: The mean effective stress is calculated on the basis of Bishop's effective stress equation with the effective stress parameter $\chi = S_r$, and the pressure is gauge pressure, which excludes atmospheric pressure (98 kPa).

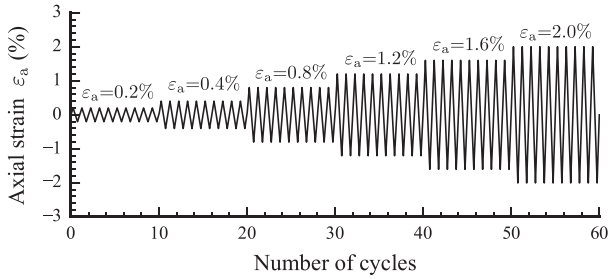

Figure 3. Time history of axial strain during cyclic shearing.

$$u_a \frac{V_a}{V_s} = u_a e(1 - S_r) = \text{constant} \tag{42}$$

A classical equation for solving problems involving three-phrase relationships (solid, water, and air) can be used to satisfy the undrained water condition as

$$w = \frac{eS_r}{G_s} = \text{constant} \tag{43}$$

where w, e, and G_s are the water content, void ratio, and specific gravity of the soil particles, respectively. As G_s is constant, we get

$$eS_r = \text{constant} \tag{44}$$

For the detailed procedure of the simulation, please refer to the Appendix A.

3.2. Model validation

The proposed constitutive model and its parameters for stress–strain characteristics (Table I) were first calibrated through undrained cyclic triaxial tests on saturated samples (case c-1), as shown in

DOI: 10.1002/nag

Figure 4. The model captures the gradual increase in the excess pore water pressure and the associated decrease in the mean effective stress, which finally leads to liquefaction after around 30 cycles of shearing. However, the decrease in the mean effective stress observed in the initial shearing cycles is, however, larger in the test. The SWCC and its parameters (Table II) were also calibrated using the water retention test under drying and wetting paths [1], as shown in Figure 5.

Next, to verify the validity of the proposed model, we conducted a series of simulations of cyclic triaxial tests on unsaturated soils under fully undrained conditions. Unno *et al*. [9] had performed cyclic triaxial tests on unsaturated samples with the same initial void ratio of 0.93 under two different initial degrees of saturation. In the simulations, the initial cyclic shearing state was first set

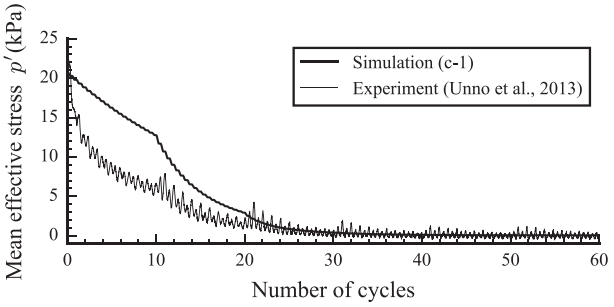

(a) Time histories of mean effective stress

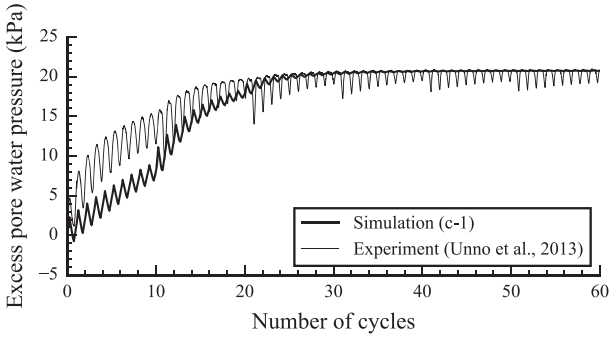

(b) Time histories of water pressure

Figure 4. Comparison between the simulation results and the experimental results of case c-1 ($S_r = 100\%$ and $e_0 = 1.09$ kPa).

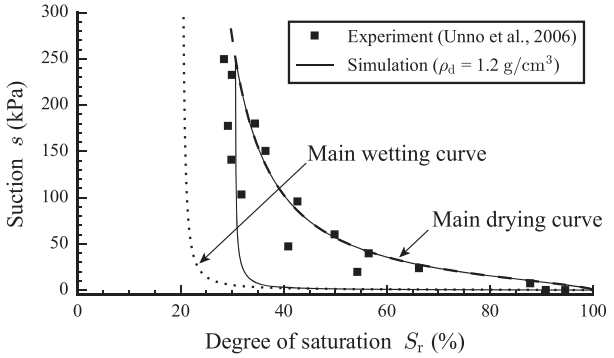

Figure 5. Comparison between the simulation results and the experimental results of the water retention test under drying and wetting paths ($\rho_d = 1.2$ g/cm^3).

DOI: 10.1002/nag

as cases c-2 and c-3 for S_r of 78.9% and 73.5%, respectively, by applying an increasing pore air pressure to an initially saturated sample under constant pore water pressure. The initial value of I_h was set to satisfy the degree of saturation and suction observed in cases c-2 and c-3. Then, cyclic shearing with a step-wise increase in axial strain amplitude, as shown in Figure 3, was applied to the specimens under unexhausted air and undrained water conditions at a constant confining pressure. Finally, the experimental results and the corresponding simulation results, that is, the time histories of mean effective stress, void ratio, air pressure, water pressure, and suction, were compared, as shown in Figures 6 and 7 for cases c-2 and c-3, respectively.

Both unsaturated soil samples lost their mean effective stress (as shown in Figures 6(a) and 7(a)) because of the development of pore air and pore water pressures [8]. The increase in pore pressure occurs because the generated excess pore pressure within the unsaturated soil cannot be drained out of the soil under fully undrained conditions.

The volumetric behavior, that is, the magnitude of the decrease in the void ratio, shown in Figures 6(b) and 7(b), was also predicted accurately. By incorporating Boyle's law, the proposed model can capture the compression behavior of unsaturated soils under fully undrained conditions. As the air pressure increases during cyclic loading, the air volume will automatically decrease following Boyle's law, as shown in Figure 8. This decrease in air volume is assumed to be equal to that of the unsaturated soils under the assumption that the soil particles and pore water are incompressible materials. In Figure 8, the dashed lines represent the inverse relationship between air void (or air content), e_a, and air pressure according to Boyle's law; in other words, the product of the air void and the absolute air pressure is constant. The simulation results indicate that the variations in air void with air pressure are consistent with Boyle's law. Moreover, the air void in case c-3 is higher than that in case c-2 at arbitrary air pressure. This is because the air void of unsaturated soil depends on the degree of saturation. At the same void ratio, the lower the degree of saturation, the higher is the air void.

In addition, the increase in the pore air pressure (as shown in Figures 6(c) and 7(c)) is higher than that in the pore water pressure (as shown in Figures 6(d) and 7(d)). As mentioned earlier, the pore air can absorb the generated excess pore pressure by compressing its volume [30]. However, the pore water is an incompressible material; hence, the generated excess pore water pressure cannot be reduced. In other words, the water void (or water content) was kept constant during the test under the undrained water condition. Figure 9 shows that the water void remains constant when the water pressure increases in cases c-2 and c-3. As with the air void, the water void of case c-3 is lower than that of case c-2 at arbitrary water pressure. This is because the water void of unsaturated soil depends on the degree of saturation. At the same void ratio, the lower the degree of saturation, the lower is the water void. Finally, this difference between the increase in the pore air pressure and the pore water pressure results in a decrease in the suction pressure under cyclic shear, as shown in Figures 6(e) and 7(e).

The proposed soil water characteristic curve model considering the effects of density and hydraulic hysteresis can also predict the increase in the degree of saturation owing to volumetric contraction [1], as shown in Figure 10.

Figures 11 and 12 show the stress–strain curve obtained from the cyclic loading simulation of unsaturated soils under fully undrained conditions for cases c-2 and c-3, respectively. It can be seen that the shear stiffness gradually decreases as the number of cycles increases. The shear strength, that is, the peak deviatoric stress, slightly increases until the third stage of cyclic shearing (20–30 cycles), but it decreases as the axial strain amplitude is increased further. Finally, the stress–strain curve becomes rather flat, at which point the liquefaction of unsaturated soil is considered to occur [31].

Figures 13 and 14 show the stress path obtained from the cyclic loading simulation of unsaturated soils under fully undrained conditions for cases c-2 and c-3, respectively. These figures indicate that the unsaturated soil loses its strength under cyclic loading in a manner similar to saturated soils.

A comparison between the simulation results and the experimental results shows that the proposed model precisely describes the cyclic behavior of unsaturated soils under fully undrained cyclic loading conditions.

DOI: 10.1002/nag

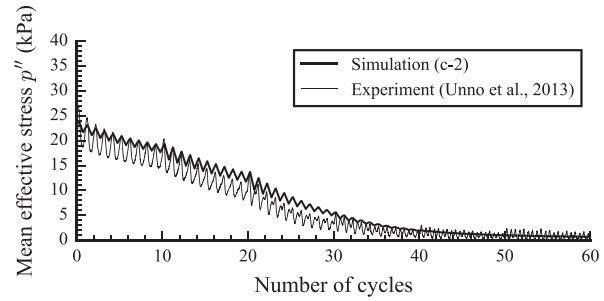

(a) Time histories of mean effective stress

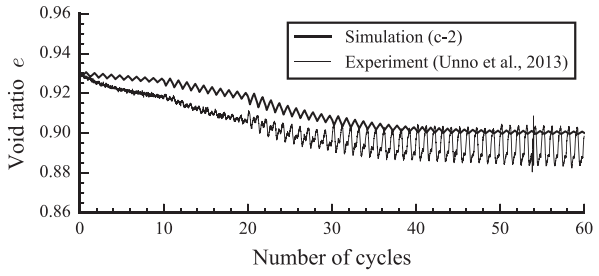

(b) Time histories of void ratio

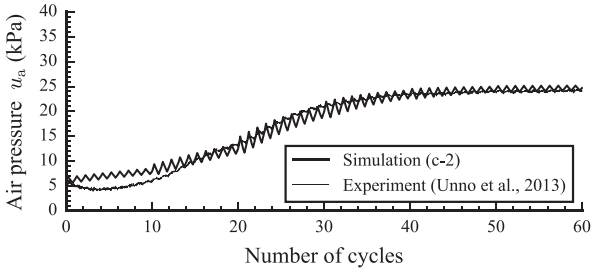

(c) Time histories of air pressure

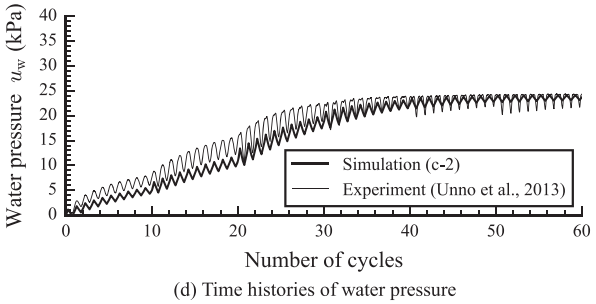

(d) Time histories of water pressure

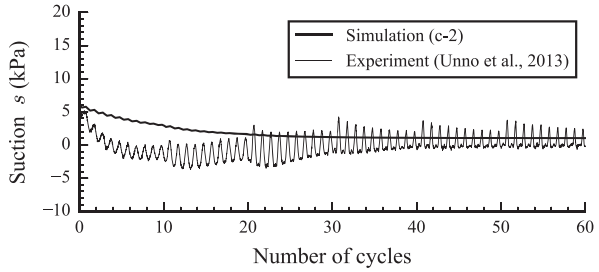

(e) Time histories of suction

Figure 6. Comparison between the simulation results and the experimental results of case c-2 (S_r = 78.9% and s = 6.0 kPa).

DOI: 10.1002/nag

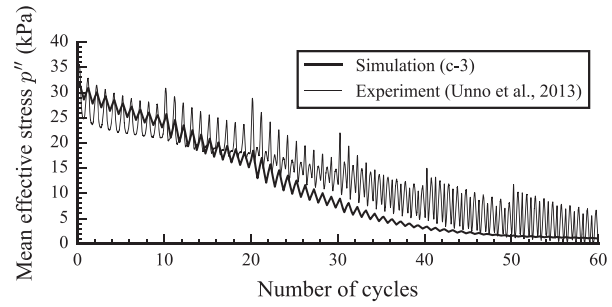

(a) Time histories of mean effective stress

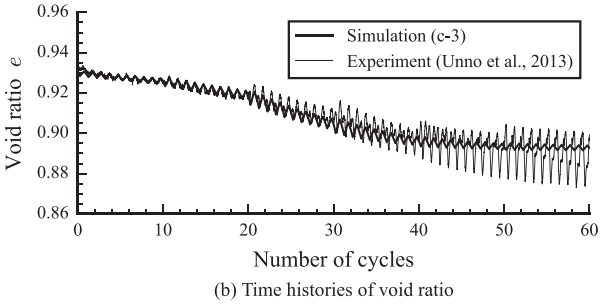

(b) Time histories of void ratio

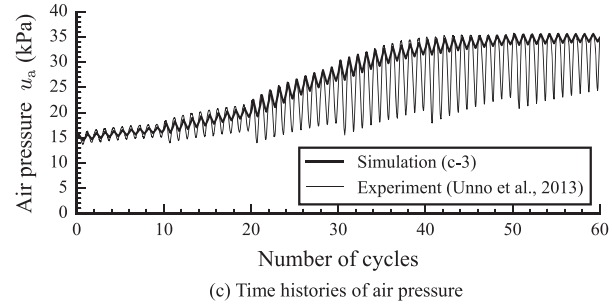

(c) Time histories of air pressure

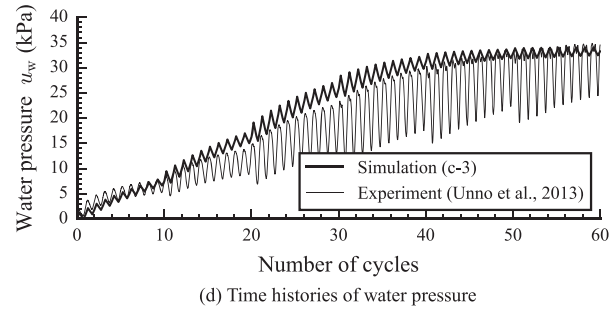

(d) Time histories of water pressure

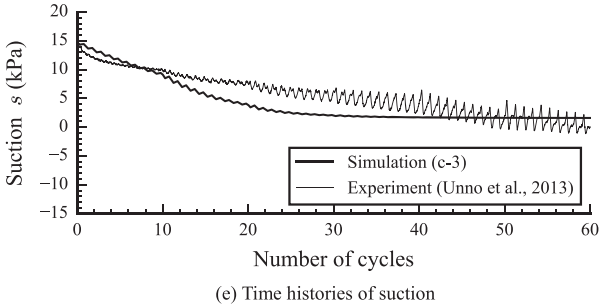

(e) Time histories of suction

Figure 7. Comparison between the simulation results and the experimental results of case c-3 (S_r = 73.5% and s = 14.8 kPa).

DOI: 10.1002/nag

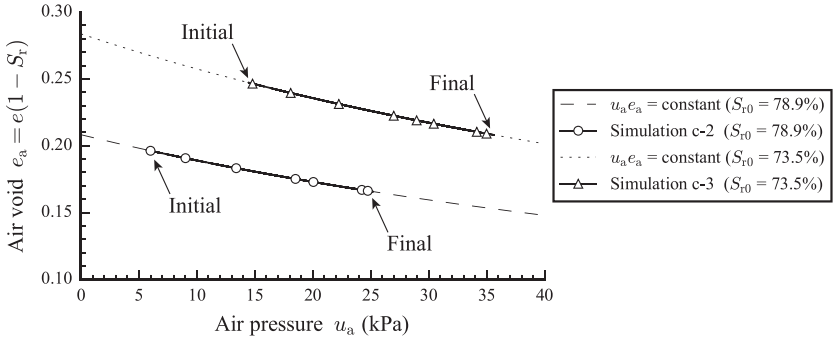

Figure 8. Relationship between air void and air pressure of cases c-2 and c-3, following Boyle's law (air pressure is gauge pressure).

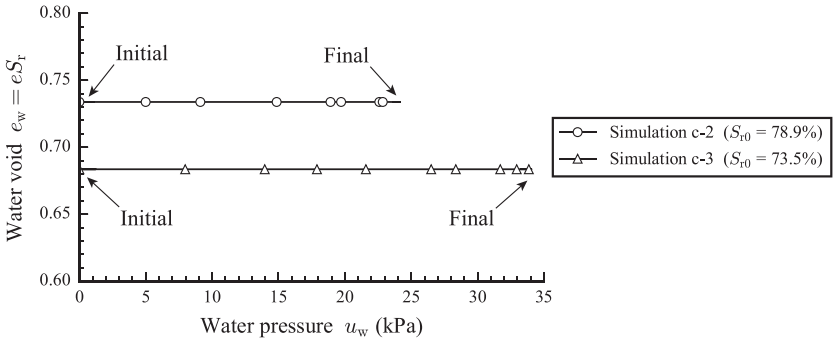

Figure 9. Relationship between water void and water pressure of cases c-2 and c-3.

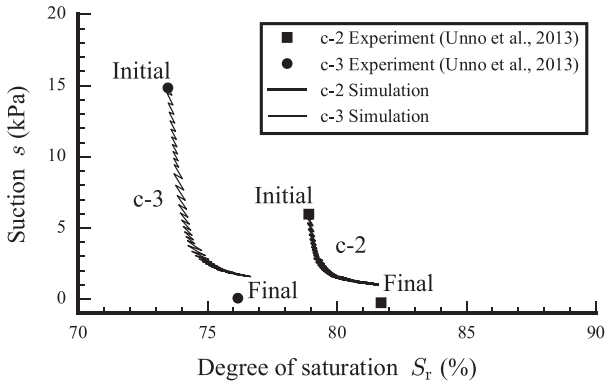

Figure 10. Increase in the degree of saturation during fully undrained cyclic triaxial tests of cases c-2 and c-3.

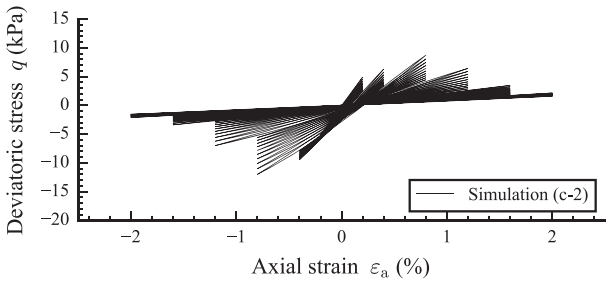

Figure 11. Stress–strain curve obtained from the cyclic loading simulation of case c-2 (S_r = 78.9% and s = 6.0 kPa).

DOI: 10.1002/nag

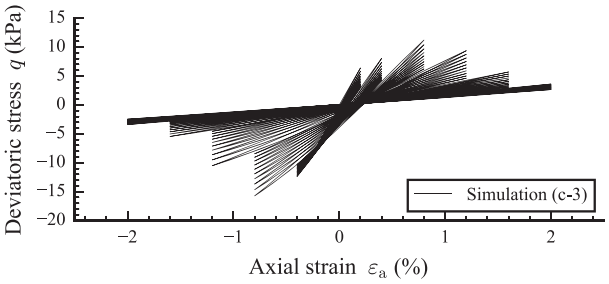

Figure 12. Stress–strain curve obtained from the cyclic loading simulation of case c-3 (S_r = 73.5% and s = 14.8 kPa).

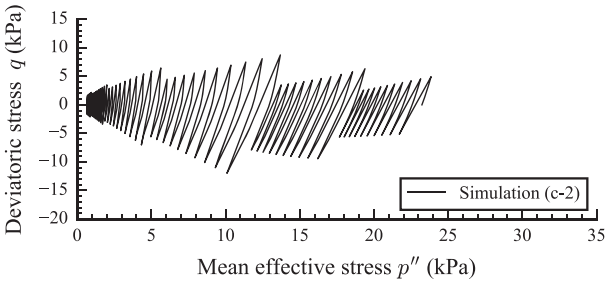

Figure 13. Stress path obtained from the cyclic loading simulation of case c-2 (S_r = 78.9% and s = 6.0 kPa).

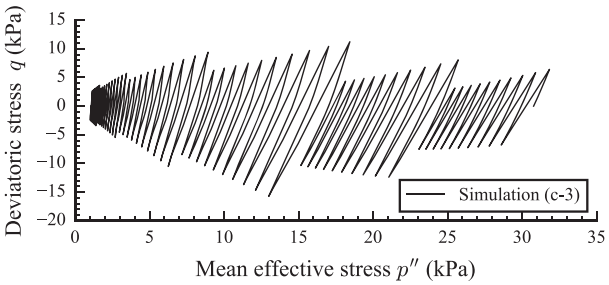

Figure 14. Stress path obtained from the cyclic loading simulation of case c-3 (S_r = 73.5%, s = 14.8 kPa).

3.3. Effects of the degree of saturation and the void ratio on the cyclic strength of unsaturated soils

A series of simulations of cyclic triaxial tests was performed on unsaturated soils using the prescribed void ratio (initial void ratio: 0.60 to 1.09) and degree of saturation (initial degree of saturation: 100% to 40%) under unexhausted air and undrained water conditions at a constant confining pressure of 20 kPa to study the effects of the degree of saturation and the void ratio on the cyclic strength of the unsaturated soils. So as to achieve the desired degree of saturation, suction was increased by decreasing the water pressure. In the simulation, the cyclic axial strain amplitude, as shown in Figure 3, was applied again to the specimens. The results of a series of simulations at a constant total confining pressure of 20 kPa are shown in Figures 15 (3D space) and 16 (2D space) for simple interpretation.

The mean effective stress reduction ratio [8] is the rate of decrease in the mean effective stress p'' of unsaturated soils after they are subjected to cyclic shear loading, and it can be used to describe the liquefaction resistance of unsaturated soils. The higher the mean effective stress reduction ratio, the lower is the liquefaction resistance of unsaturated soils.

DOI: 10.1002/nag

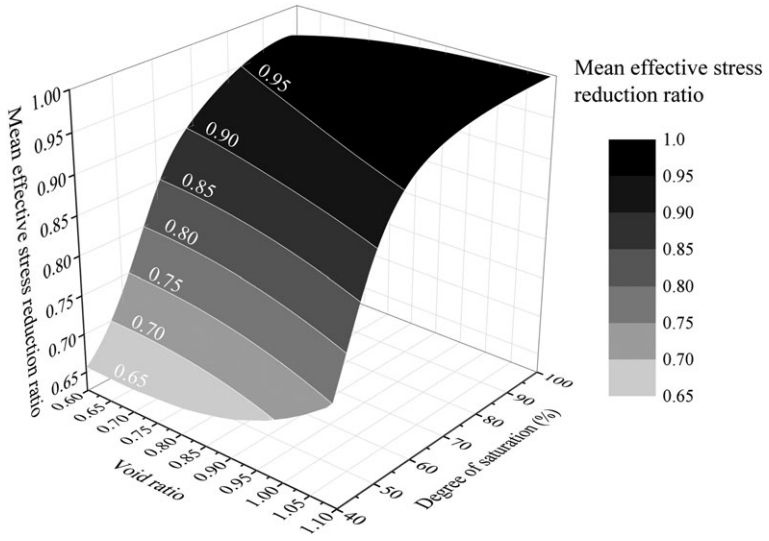

Figure 15. Three-dimensional surface of cyclic strength of unsaturated soils: effect of degree of saturation and void ratio (constant total confining pressure of 20 kPa).

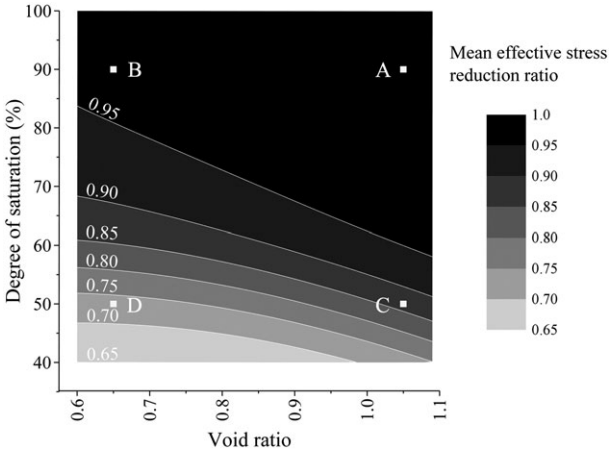

Figure 16. Effect of void ratio and degree of saturation on the cyclic strength of unsaturated soils (constant total confining pressure of 20 kPa).

$$\text{Mean effective stress reduction ratio} = 1 - \frac{p''}{p''_0} \tag{45}$$

The mean effective stress reduction ratio is equal to 1 in the complete liquefaction state.

Points A, B, C, and D in Figure 16 represent examples of unsaturated soils having different initial degrees of saturation and void ratios: A represents loose unsaturated soil with a high degree of saturation (S_{r0} = 90%, e_0 = 1.05); B represents dense unsaturated soil with a high degree of saturation (S_{r0} = 90%, e_0 = 0.65); C represents loose unsaturated soil with a low degree of saturation (S_{r0} = 50%, e_0 = 1.05); and D represents dense unsaturated soil with a low degree of saturation (S_{r0} = 50%, e_0 = 0.65).

All the specimens experience a reduction in the mean effective stress during cyclic shearing simulation, and specimen A, which is a loose unsaturated soil with a high degree of saturation, is finally liquefied after approximately 38 cycles, as shown in Figure 17. The cyclic strength of unsaturated soils can be evaluated by the mean effective stress reduction ratio, as shown in Figure 18. Specimen A shows a drastic loss in mean effective stress compared with the other

DOI: 10.1002/nag

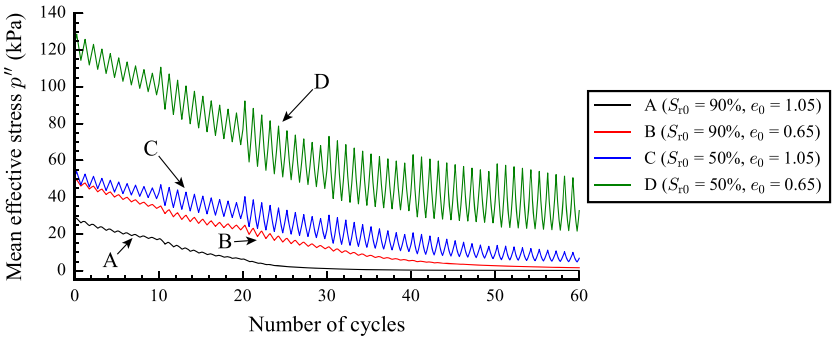

Figure 17. Time histories of mean effective stress at points A, B, C, and D (as shown in Figure 16). [Colour figure can be viewed at wileyonlinelibrary.com]

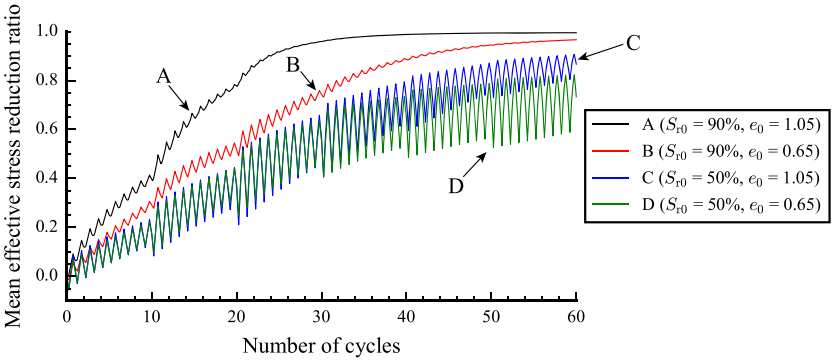

Figure 18. Time histories of mean effective stress reduction ratio at points A, B, C, and D (as shown in Figure 16). [Colour figure can be viewed at wileyonlinelibrary.com]

specimens, and its mean effective stress reduction ratio reaches 1.0 after around 38 cycles. For specimen B, which has a high degree of saturation and high density, the mean effective stress reduction ratio nearly reaches 1.0 at the end of the simulation. However, even though specimens C and D, which have low degrees of saturation, show a decrease in shear strength as the mean effective stress decreases, they are not liquefied during the cyclic shearing simulation.

Figure 19 shows the variation in the void ratio during the simulation. The void ratios of specimens A and B remain nearly constant. This is because a change in the volume of the unsaturated soils under fully undrained conditions depends only on the volume of air. Specimens A and B have a high degree of saturation; therefore, the volume of air that affects the variation in the void ratio is limited. On the other hand, the variations in the void ratios of specimens C and D are higher than those of

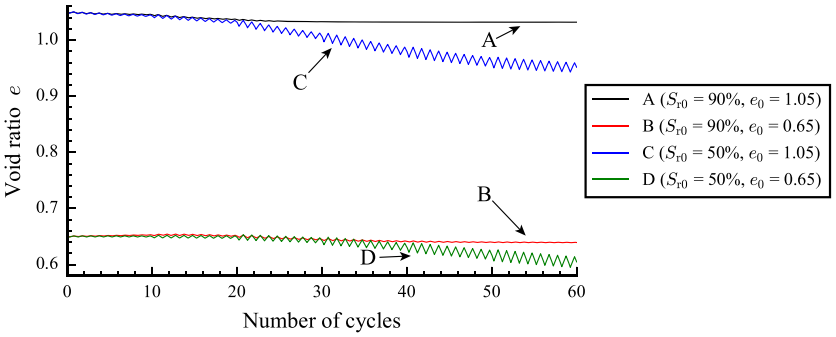

Figure 19. Time histories of void ratio at points A, B, C, and D (as shown in Figure 16). [Colour figure can be viewed at wileyonlinelibrary.com]

DOI: 10.1002/nag

specimen A and B because specimens C and D have a low degree of saturation. As shown in Figure 20, Specimens A and C, which are loose unsaturated soils, exhibit compression behavior during the cyclic shearing simulation. However, the normalized void ratio of specimen A becomes constant as it approaches the liquefaction state while that of specimen C continuously decreases until the end of the simulation. Specimens B and D, which are dense unsaturated soils, exhibit dilatancy at the beginning of the simulation, followed by compression behavior. It is also seen that the normalized void ratio of specimen B becomes nearly constant as it approaches the liquefaction state.

The pore air pressure and the pore water pressure of all the specimens increased during the simulation, as shown in Figures 21 and 22, respectively. However, there was a decrease in the air pressure of specimens B and D in the first 10 cycles, because the variation in the air pressure is inversely proportional to the variation in the void ratio, as per Boyle's law (Equation (3)). Moreover, the pore

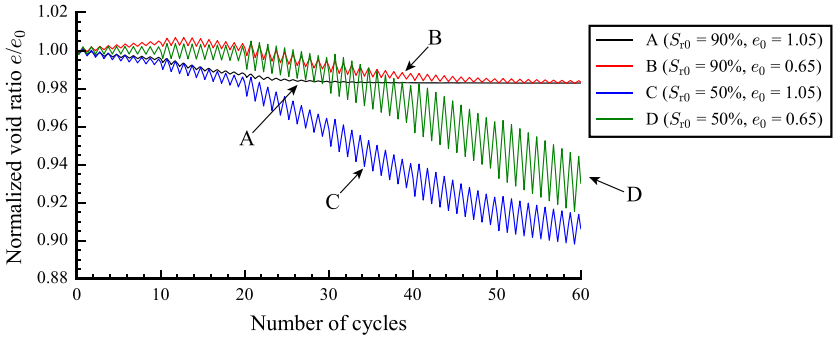

Figure 20. Time histories of normalized void ratio at points A, B, C, and D (as shown in Figure 16). [Colour figure can be viewed at wileyonlinelibrary.com]

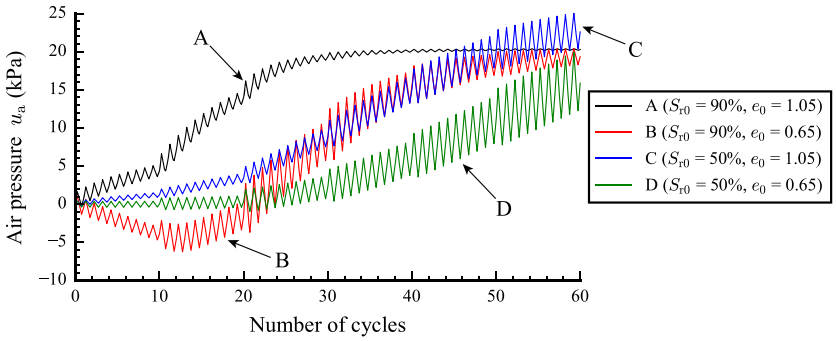

Figure 21. Time histories of air pressure at points A, B, C, and D (as shown in Figure 16). [Colour figure can be viewed at wileyonlinelibrary.com]

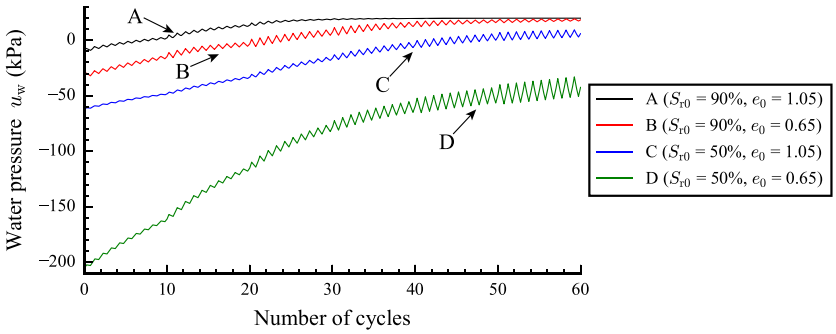

Figure 22. Time histories of water pressure at points A, B, C, and D (as shown in Figure 16). [Colour figure can be viewed at wileyonlinelibrary.com]

DOI: 10.1002/nag

air pressure and the pore water pressure of specimen A stopped increasing after around 38 cycles, once the liquefaction state was reached, as did those of specimen B at the end of the simulation.

Figure 23 show the suction decreased in all the specimens. However, the reduction rate of the suction in specimens A and B was significantly higher than that in specimens C and D, as shown in Figure 24. This is because specimens A and B had a higher degree of saturation than specimens C and D; moreover, the initial pore air pressure and the initial pore water pressure were closer to each other in specimens A and B than in specimens C and D. This reduction in suction, which depends on the initial degree of saturation, was also observed in the experimental results obtained by Unno *et al*. [1] and Liu and Xu [6].

Furthermore, this result can be explained by the following factors. Based on the volumetric movement of the state boundary surface owing to the variation in the degree of saturation, unsaturated soils behave more similarly to dense soils, which gain cyclic strength owing to their dilatancy characteristics [31]. Figures 25 and 26 show examples of the stress–strain curve obtained

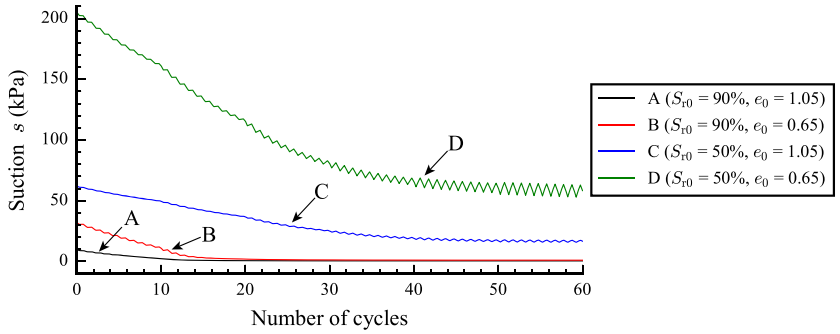

Figure 23. Time histories of suction at points A and B (as shown in Figure 16). [Colour figure can be viewed at wileyonlinelibrary.com]

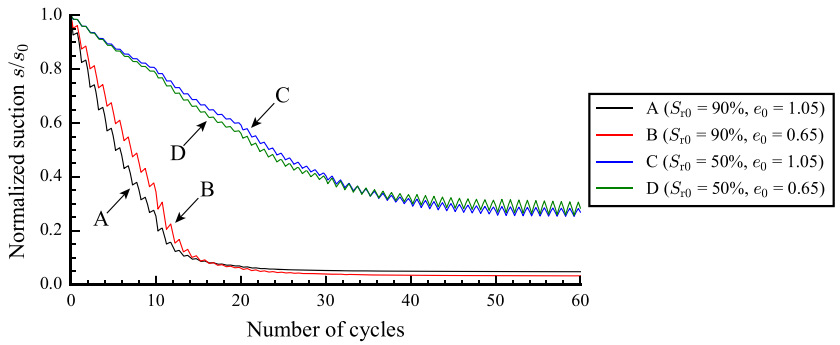

Figure 24. Time histories of normalized suction at points A and B (as shown in Figure 16). [Colour figure can be viewed at wileyonlinelibrary.com]

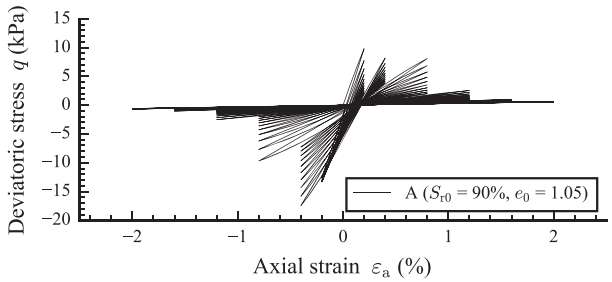

Figure 25. Stress–strain curve obtained from specimen A (as shown in Figure 16).

DOI: 10.1002/nag

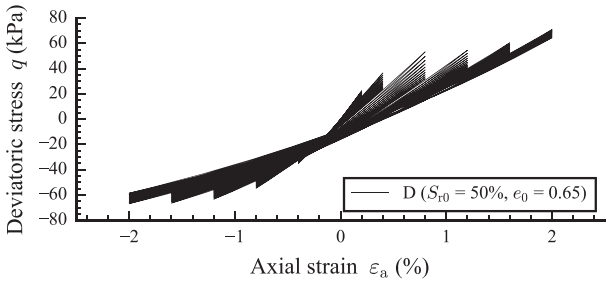

Figure 26. Stress–strain curve obtained from specimen D (as shown in Figure 16).

from specimens A and D; under cyclic loading, the cyclic strength decreases as the number of cycles increases in both cases. When the initial degree of saturation is high, the peak deviatoric stress decreases as the axial strain increases owing to the compression behavior, as shown in Figure 25. On the other hand, the peak deviatoric stress of unsaturated soils having a low initial degree of saturation increases with the axial strain owing to their dilatancy characteristics, as shown in Figure 26. Furthermore, unsaturated soils with a low degree of saturation have a low volume of pore air to absorb the generated excess pore pressure [30], as discussed in Section 3.2.

In conclusion, the liquefaction resistance of unsaturated soils increases as the degree of saturation and void ratio decrease. However, the degree of saturation has a greater effect than the void ratio on the liquefaction resistance of unsaturated soils.

3.4. Effects of the confining pressure on the cyclic strength of unsaturated soils

To consider the effect of the confining pressure on the cyclic strength of unsaturated soils, we performed a series of simulations of cyclic triaxial tests on the specimens of unsaturated soils under unexhausted air and undrained water conditions at a constant total confining pressure varying from 20 to 300 kPa. In the simulations, each saturated specimen with an initial void ratio of 1.09 was first consolidated from 20 kPa to the desired confining pressure up to 300 kPa. Suction was then applied to each specimen by decreasing the water pressure until the desired initial degree of saturation, varying from 40% to 100%, was reached. Subsequently, cyclic axial strain was applied to all the specimens under fully undrained conditions at a constant total confining pressure, as shown in Figure 3. The results of the simulations are shown in Figures 27 (3D space) and 28 (2D space) for simple interpretation.

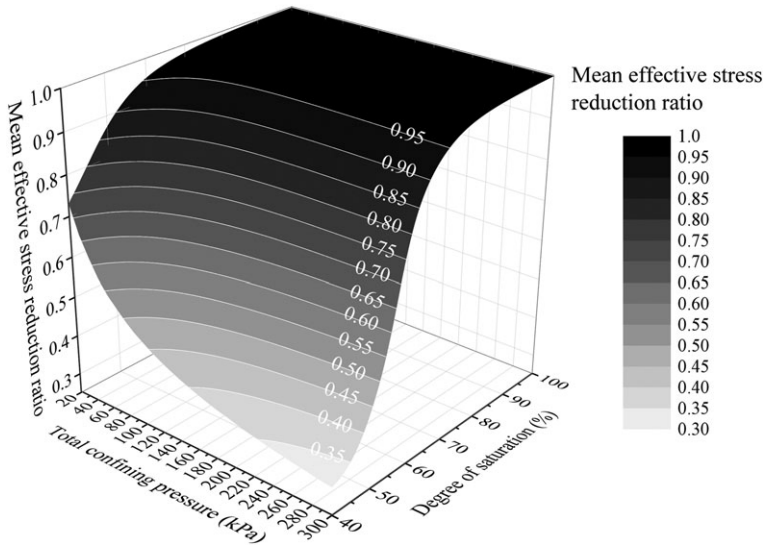

Figure 27. Three-dimensional surface of cyclic strength of unsaturated soils: effect of confining pressure and degree of saturation.

DOI: 10.1002/nag

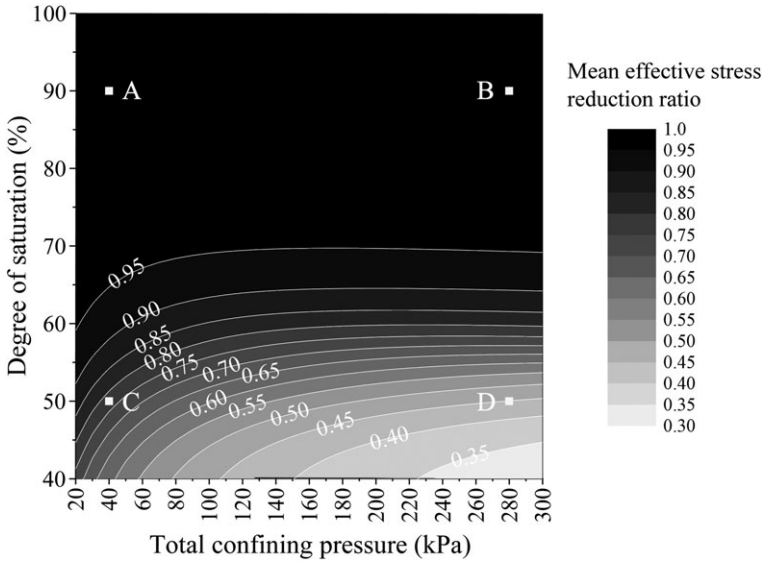

Figure 28. Effect of confining pressure and degree of saturation on the cyclic strength of unsaturated soils.

Points A, B, C, and D in Figure 28 represent examples of unsaturated soils having different initial degrees of saturation and total confining pressures: A represents unsaturated soil with a high degree of saturation and low total confining pressure (S_{r0} = 90% and σ_{c0} = 40 kPa); B represents unsaturated soil with a high degree of saturation and high total confining pressure (S_{r0} = 90% and σ_{c0} = 280 kPa); C represents unsaturated soil with a low degree of saturation and low total confining pressure (S_{r0} = 50% and σ_{c0} = 40 kPa); and D represents unsaturated soil with a low degree of saturation and high total confining pressure (S_{r0} = 50% and σ_{c0} = 280 kPa).

All the specimens lost their mean effective stress during the cyclic shearing simulation, in which specimens A and B liquefied after around 28 and 40 cycles, respectively, as shown in Figure 29. However, as shown in Figure 30, the mean effective stress reduction ratio of specimen A was nearly the same as that of specimen B, which is higher than that of specimens C and D. This indicates that the cyclic strength of unsaturated soils is highly dependent on the degree of saturation, while the effect of the total confining pressure on the cyclic strength of unsaturated soils is more evident at lower degrees of saturation. These simulation results are in good agreement with the experimental results obtained by Liu and Xu [6].

Figure 31 shows the variation in the void ratio during the simulation. The initial void ratio of specimens A and C is higher than those of specimens B and D because of the total confining pressure. As discussed in Section 3.3, the void ratio of specimens A and B remains nearly constant, while specimens C and D show a greater reduction in the void ratio during the simulation owing to

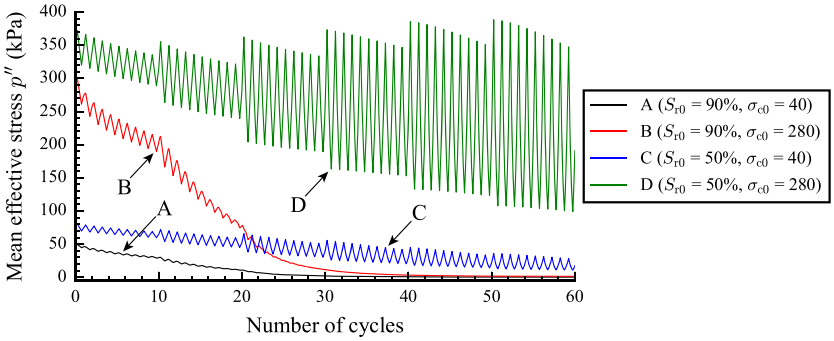

Figure 29. Time histories of mean effective stress at points A, B, C, and D (as shown in Figure 28). [Colour figure can be viewed at wileyonlinelibrary.com]

DOI: 10.1002/nag

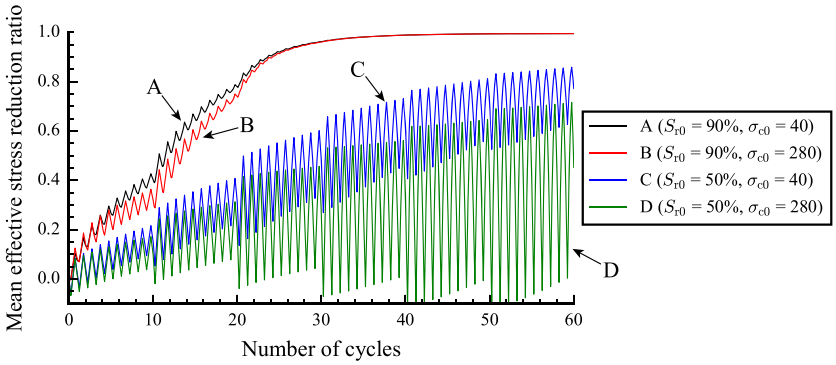

Figure 30. Time histories of mean effective stress reduction ratio at points A, B, C, and D (as shown in Figure 28). [Colour figure can be viewed at wileyonlinelibrary.com]

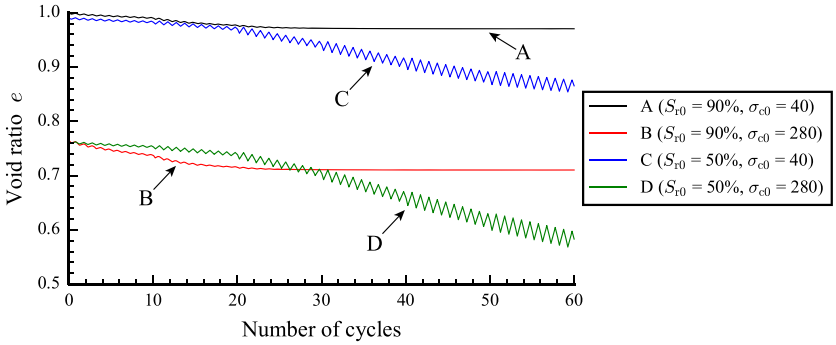

Figure 31. Time histories of void ratio at points A, B, C, and D (as shown in Figure 28). [Colour figure can be viewed at wileyonlinelibrary.com]

the difference in the initial degrees of saturation. However, if we consider only the effect of the total confining pressure on the variation in the void ratio by using the normalized void ratio at different degrees of saturation, as shown in Figure 32, then it can be seen that the higher the confining pressure, the higher is the compression rate of the void ratio. Specimens A, B, C, and D are found to exhibit compression behavior during the fully undrained cyclic loading simulation even though specimens B and D are dense soils, because dense soils usually show compression behavior under low strain, followed by dilation behavior at higher strain. Therefore, it is possible that dense soils will show only compression behavior if they are subjected to low strain [6].

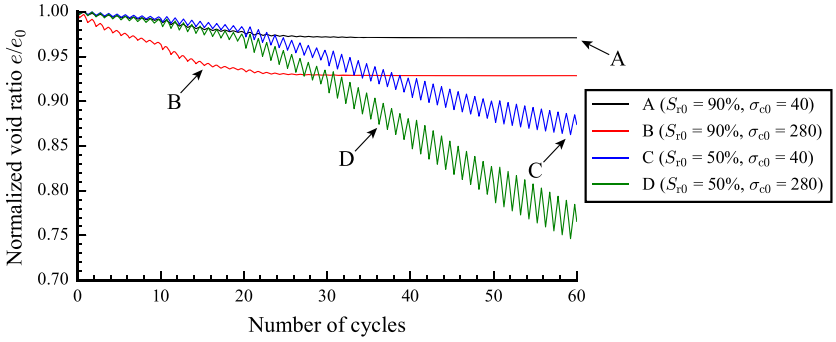

Figure 32. Time histories of normalized void ratio at points A, B, C, and D (as shown in Figure 28). [Colour figure can be viewed at wileyonlinelibrary.com]

DOI: 10.1002/nag

The pore air pressure and the pore water pressure of all the specimens increased during the simulation owing to the decrease in the void ratio (as shown in Figures 33 and 34, respectively). At each degree of saturation, it is seen that an increase in the pore air pressure and the pore water pressure depends on the total confining pressure. The higher the total confining pressure, the higher is the increase in the pore air and pore water pressures. Moreover, the pore air pressure and the pore water pressure of specimens A and B stopped increasing after reaching the total confining pressure. In this state, specimens A and B were completely liquefied. This development in the pore air and pore water pressures leads to a decrease in the mean effective stress of unsaturated soils, as mentioned earlier.

The initial suction of each specimen was different depending on the desired degree of saturation, as shown in Figure 35. It is seen that the suction in all the specimens decreased during the simulation.

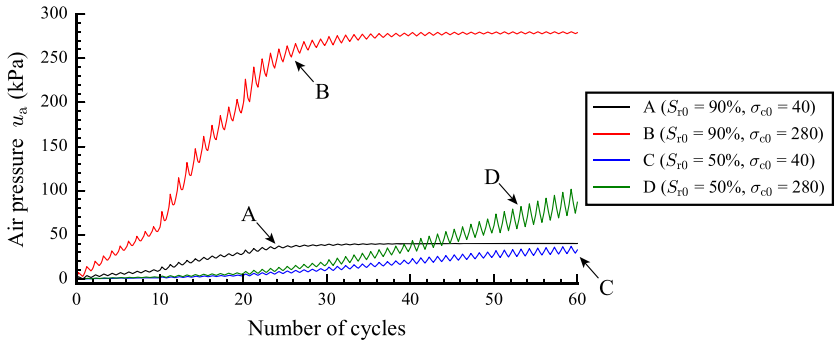

Figure 33. Time histories of air pressure at points A, B, C, and D (as shown in Figure 28). [Colour figure can be viewed at wileyonlinelibrary.com]

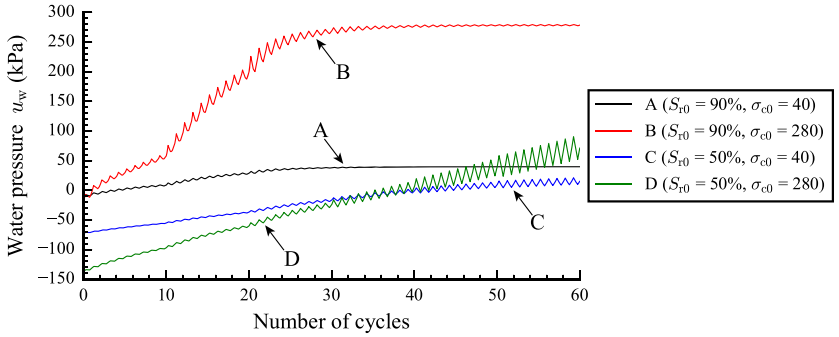

Figure 34. Time histories of water pressure at points A, B, C, and D (as shown in Figure 28). [Colour figure can be viewed at wileyonlinelibrary.com]

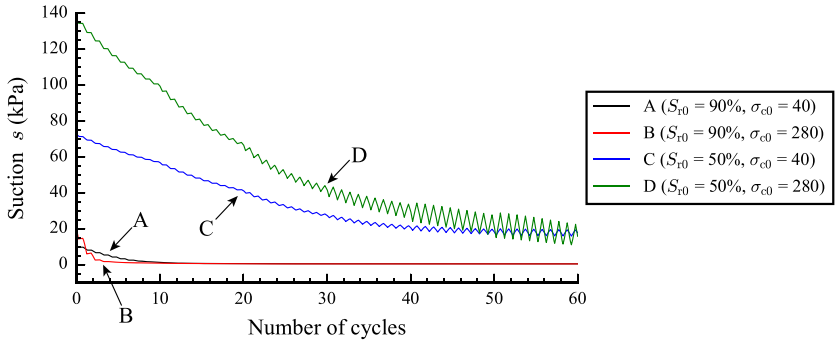

Figure 35. Time histories of suction at points A and B (as shown in Figure 28). [Colour figure can be viewed at wileyonlinelibrary.com]

DOI: 10.1002/nag

Moreover, the reduction rate of suction of specimens with higher total confining pressure is higher than that of specimens with lower total confining pressure, as shown in Figure 36.

Figure 37 shows the stress–strain curves obtained from specimens C and D. At the same initial degree of saturation, the deviatoric stress of specimen C was less than that of specimen D under the same axial strain level. It can be concluded that the deviatoric stress of unsaturated soils increases with the total confining pressure under the same initial degree of saturation. A stronger soil naturally experiences a higher deviatoric stress than a weaker soil under the same axial strain level. Thus, the higher the confining pressure, the higher is the cyclic strength of the soil.

In conclusion, the liquefaction resistance of unsaturated soils increases with the total confining pressure. However, as indicated by the simulation using the parameters of Tsukidate volcanic sand with cyclic loading history shown in Figure 3 that the effect of the total confining pressure on the cyclic strength of unsaturated soils is insignificant when the degree of saturation is higher than 70%, whereas it is more evident at lower degrees of saturation. Furthermore, the unsaturated soils are observed to easily liquefy when the degree of saturation is higher than 70% (i.e., when the mean effective stress reduction ratio is higher than 0.9), regardless of the initial confining pressure.

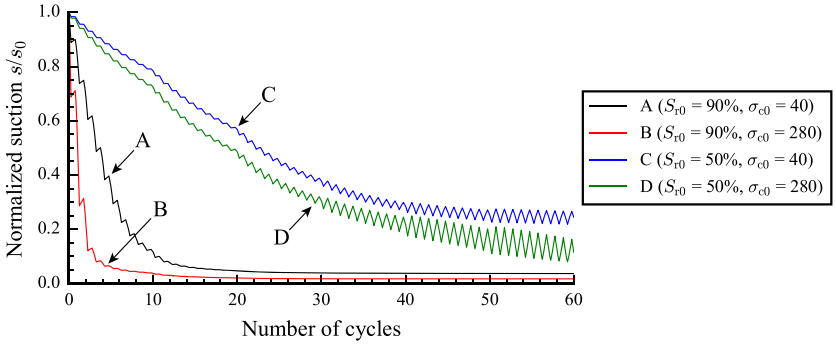

Figure 36. Time histories of normalized suction at points A and B (as shown in Figure 28). [Colour figure can be viewed at wileyonlinelibrary.com]

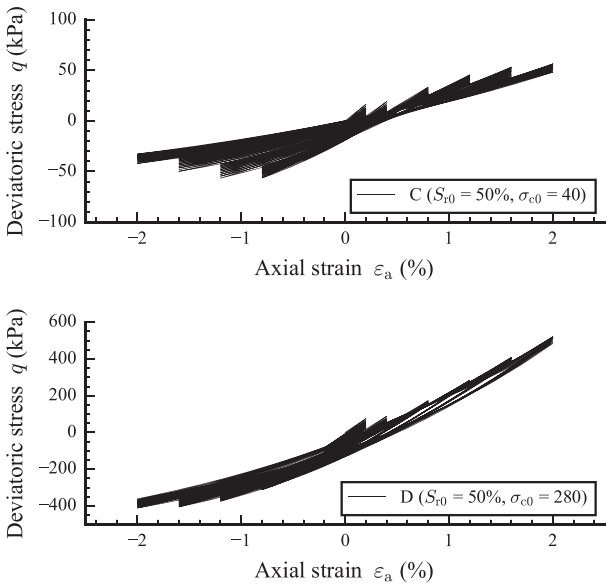

Figure 37. Stress–strain curves obtained from specimens C and D (as shown in Figure 28).

DOI: 10.1002/nag

4. CONCLUSIONS

This paper proposed a three-dimensional extension of an elastoplastic model for unsaturated soils. This model was formulated on the basis of a critical state soil model, that is, the modified Cam clay model, using effective stress tensor for unsaturated soils, which incorporates the following concepts: the volumetric movement of the state boundary surface containing the CSL owing to the variation in the degree of saturation; the soil water characteristic curve model considering the effects of specific volume and hydraulic hysteresis; and the subloading surface concept. The volumetric behavior of the void air was modeled by Boyle's law.

The validity of the proposed model was verified through a series of cyclic triaxial tests on saturated and unsaturated soils under fully undrained conditions. The results showed that the proposed model properly describes the fully undrained cyclic behavior of unsaturated soils, such as liquefaction, compression associated with Boyle's law, and an increase in the degree of saturation owing to a decrease in suction and volumetric compression.

The results also showed that unsaturated soils with a low degree of saturation and low void ratio have high cyclic strength. Moreover, the cyclic strength increases with the total confining pressure. Among various factors, the degree of saturation has a significant effect on the liquefaction resistance of unsaturated soils.

In the future, we plan to solve the initial/boundary value problem of unsaturated reclaimed ground under earthquake-induced cyclic loading by using a finite element method based on the critical state model for unsaturated soils proposed in this study. Thus, we expect to obtain information about the effect of cyclic loading on unsaturated soil layers in practical situations.

APPENDIX A.
RATE FORM OF THE STRESS–STRAIN RELATIONSHIP

The proposed model is capable of describing the behavior of unsaturated soils under various testing conditions, for example, fully drained condition, constant water content condition, and fully undrained condition. The constitutive equations of the proposed model are presented herein.

First, substituting the time derivative of effective stress tensor for unsaturated soils, as shown in Equation (2), into Equation (38) gives

$$\dot{\boldsymbol{\sigma}}^{\mathrm{net}} + S_{\mathrm{r}}\mathbf{1}\dot{s} + s\mathbf{1}\dot{S}_{\mathrm{r}} = \boldsymbol{D}^{\mathrm{ep}} : \dot{\boldsymbol{\varepsilon}} - \boldsymbol{D}^{\mathrm{Sr}}\dot{S}_{\mathrm{r}} \tag{A-1}$$

where $\dot{\boldsymbol{\sigma}}^{\mathrm{net}}$ and $\dot{s}$ are the rate of Cauchy's net stress tensor and suction, respectively. Assuming incompressibility of soil particles, we obtain $\dot{e} = -v_0\mathbf{1} : \dot{\boldsymbol{\varepsilon}}$. Substituting this into Equation (12), we obtain

$$\dot{S}_{\mathrm{r}} = \frac{\dfrac{\partial S_{\mathrm{r}}}{\partial s}\dot{s} - \dfrac{\partial S_{\mathrm{r}}}{\partial e}v_0\mathbf{1} : \dot{\boldsymbol{\varepsilon}}}{1 - \dfrac{\partial S_{\mathrm{r}}\mathrm{d}I_{\mathrm{h}}}{\partial I_{\mathrm{h}}\mathrm{d}S_{\mathrm{r}}}} \tag{A-2}$$

Substituting the rate of the degree of saturation $\dot{S}_{\mathrm{r}}$ into Equation (A-1) gives

$$\dot{\boldsymbol{\sigma}}^{\mathrm{net}} = \boldsymbol{D}^{\mathrm{ep}} : \dot{\boldsymbol{\varepsilon}} - S_{\mathrm{r}}\mathbf{1}\dot{s} - \left(\boldsymbol{D}^{\mathrm{Sr}} + s\mathbf{1}\right)\frac{\dfrac{\partial S_{\mathrm{r}}}{\partial s}\dot{s} - \dfrac{\partial S_{\mathrm{r}}}{\partial e}v_0\mathbf{1} : \dot{\boldsymbol{\varepsilon}}}{1 - \dfrac{\partial S_{\mathrm{r}}\mathrm{d}I_{\mathrm{h}}}{\partial I_{\mathrm{h}}\mathrm{d}S_{\mathrm{r}}}} \tag{A-3}$$

Equation (A-3) can be rearranged as

$$\dot{\boldsymbol{\sigma}}^{\mathrm{net}} = \boldsymbol{D}^{\mathrm{net}} : \dot{\boldsymbol{\varepsilon}} - \boldsymbol{D}^{\mathrm{s}}\dot{s} \tag{A-4}$$

DOI: 10.1002/nag

where $\boldsymbol{D}^{\mathrm{net}}$ and $\boldsymbol{D}^{\mathrm{s}}$ are defined by

$$\boldsymbol{D}^{\mathrm{net}} = \boldsymbol{D}^{\mathrm{ep}} + \left(\boldsymbol{D}^{\mathrm{Sr}} + s\mathbf{1}\right) \otimes \frac{\dfrac{\partial S_{\mathrm{r}}}{\partial e} v_0 \mathbf{1}}{1 - \dfrac{\partial S_{\mathrm{r}} \mathrm{d}I_{\mathrm{h}}}{\partial I_{\mathrm{h}} \mathrm{d}S_{\mathrm{r}}}} \tag{A-5}$$

$$\boldsymbol{D}^{\mathrm{s}} = S_{\mathrm{r}}\mathbf{1} + \left(\boldsymbol{D}^{\mathrm{Sr}} + s\mathbf{1}\right) \frac{\dfrac{\partial S_{\mathrm{r}}}{\partial s}}{1 - \dfrac{\partial S_{\mathrm{r}} \mathrm{d}I_{\mathrm{h}}}{\partial I_{\mathrm{h}} \mathrm{d}S_{\mathrm{r}}}} \tag{A-6}$$

Substituting $\dot{\boldsymbol{\sigma}}^{\mathrm{net}} = \dot{\boldsymbol{\sigma}} - \dot{u_{\mathrm{a}}}\mathbf{1}$ and $\dot{s} = \dot{u_{\mathrm{a}}} - \dot{u_{\mathrm{w}}}$ into Equation (A-4), we obtain

$$\dot{\boldsymbol{\sigma}} = \boldsymbol{D}^{\mathrm{net}} : \dot{\boldsymbol{\varepsilon}} + (\mathbf{1} - \boldsymbol{D}^{\mathrm{s}})\dot{u_{\mathrm{a}}} + \boldsymbol{D}^{\mathrm{s}}\dot{u_{\mathrm{w}}} \tag{A-7}$$

where $\dot{u_{\mathrm{a}}}$ and $\dot{u_{\mathrm{w}}}$ are the rates of air pressure and water pressure, respectively.

Drainage conditions for elementary tests

The testing conditions for predicting unsaturated soil behavior are varied according to the drainage conditions of pore air and pore water, namely exhausted air condition, unexhausted air condition, drained water condition, or undrained water condition.

The exhausted air condition is the condition that air is able to drain out of the soil. Therefore, we usually assume that there is no change in air pressure. In other words, the increment in air pressure is constant, which can be written as

$$\dot{u_{\mathrm{a}}} = 0 \text{ (Exhausted air condition)} \tag{A-8}$$

The drained water condition is the condition that pore water is able to drain out of the soil. Therefore, we usually assume that there is no change in water pressure. In other words, the increment in water pressure is constant, which can be written as

$$\dot{u_{\mathrm{w}}} = 0 \text{ (Drained water condition)} \tag{A-9}$$

The unexhausted air condition is the condition that air is unable to drain out of the soil. In other words, the mass of air is constant. We assume that air is an ideal gas and the temperature is constant. Thus, Boyle's law can be applied here as

$$\left(V_{\mathrm{a}}\dot{u_{\mathrm{a}}}\right) = 0 \text{ (Unexhausted air condition)} \tag{A-10}$$

where V_{a} is the volume of void air. As the volume of soil particles, V_{s}, is assumed to be constant and as $\frac{V_{\mathrm{a}}}{V_{\mathrm{s}}} = e(1 - S_{\mathrm{r}})$, we obtain

$$\left\{e(1 - \dot{S}_{\mathrm{r}})u_{\mathrm{a}}\right\} = 0. \tag{A-11}$$

Solving Equation (A-11), we obtain the constraint for the unexhausted air condition as

$$\dot{S_{\mathrm{r}}} = (1 - S_{\mathrm{r}})\frac{\dot{u_{\mathrm{a}}}}{u_{\mathrm{a}}} + (1 - S_{\mathrm{r}})\frac{\dot{e}}{e} \tag{A-12}$$

where $\dot{e} = -v_0\mathbf{1} : \dot{\boldsymbol{\varepsilon}}$. Substituting Equation (A-12) into (A-2), we obtain

$$(1 - S_{\mathrm{r}})\frac{\dot{u_{\mathrm{a}}}}{u_{\mathrm{a}}} - (1 - S_{\mathrm{r}})\frac{v_0\mathbf{1} : \dot{\boldsymbol{\varepsilon}}}{e} = \frac{\dfrac{\partial S_{\mathrm{r}}}{\partial s}\dot{s} - \dfrac{\partial S_{\mathrm{r}}}{\partial e} v_0\mathbf{1} : \dot{\boldsymbol{\varepsilon}}}{1 - \dfrac{\partial S_{\mathrm{r}} \mathrm{d}I_{\mathrm{h}}}{\partial I_{\mathrm{h}} \mathrm{d}S_{\mathrm{r}}}} \tag{A-13}$$

where $\dot{s} = \dot{u_{\mathrm{a}}} - \dot{u_{\mathrm{w}}}$. Equation (A-13) can be rearranged as

DOI: 10.1002/nag

$$\left[\frac{\partial S_{\mathrm{r}}}{\partial e}+\left(1-\frac{\partial S_{\mathrm{r}}\mathrm{d}I_{\mathrm{h}}}{\partial I_{\mathrm{h}}\mathrm{d}S_{\mathrm{r}}}\right)\frac{(S_{\mathrm{r}}-1)}{e}\right]v_0\mathbf{1}:\dot{\boldsymbol{\varepsilon}}=\left[\left(1-\frac{\partial S_{\mathrm{r}}\mathrm{d}I_{\mathrm{h}}}{\partial I_{\mathrm{h}}\mathrm{d}S_{\mathrm{r}}}\right)\frac{(S_{\mathrm{r}}-1)}{u_{\mathrm{a}}}+\frac{\partial S_{\mathrm{r}}}{\partial s}\right]\dot{u_{\mathrm{a}}}-\frac{\partial S_{\mathrm{r}}}{\partial s}\dot{u_{\mathrm{w}}} \tag{A-14}$$

The undrained water condition is the condition that water is unable to drain out of the soil. In other words, the mass of water is constant. Therefore, taking the time derivative of water content w gives

$$\dot{w}=(e\dot{S_{\mathrm{r}}})=0\ (\text{Undrained water condition}). \tag{A-15}$$

Thus, we get the constraint for the undrained water condition as

$$\dot{S_{\mathrm{r}}}=-\frac{S_{\mathrm{r}}\dot{e}}{e} \tag{A-16}$$

where $\dot{e}=-v_0\mathbf{1}:\dot{\boldsymbol{\varepsilon}}$. Substituting Equation (A-16) into (A-2), we obtain

$$\frac{S_{\mathrm{r}}v_0\mathbf{1}:\dot{\boldsymbol{\varepsilon}}}{e}=\frac{\dfrac{\partial S_{\mathrm{r}}}{\partial s}\dot{s}-\dfrac{\partial S_{\mathrm{r}}}{\partial e}v_0\mathbf{1}:\dot{\boldsymbol{\varepsilon}}}{1-\dfrac{\partial S_{\mathrm{r}}\mathrm{d}I_{\mathrm{h}}}{\partial I_{\mathrm{h}}\mathrm{d}S_{\mathrm{r}}}} \tag{A-17}$$

where $\mathrm{d}s=\mathrm{d}u_{\mathrm{a}}-\mathrm{d}u_{\mathrm{w}}$. Equation (A-17) can be rearranged as

$$\left[\left(1-\frac{\partial S_{\mathrm{r}}\mathrm{d}I_{\mathrm{h}}}{\partial I_{\mathrm{h}}\mathrm{d}S_{\mathrm{r}}}\right)\left(\frac{S_{\mathrm{r}}}{e}\right)+\frac{\partial S_{\mathrm{r}}}{\partial e}\right]v_0\mathbf{1}:\dot{\boldsymbol{\varepsilon}}=\frac{\partial S_{\mathrm{r}}}{\partial s}\dot{u_{\mathrm{a}}}-\frac{\partial S_{\mathrm{r}}}{\partial s}\dot{u_{\mathrm{w}}}. \tag{A-18}$$

Constitutive relationship for exhausted air and drained water condition (fully drained condition)

The fully drained condition, that is, exhausted air and drained water, is the condition that air and water are able to drain out of the soil. So as to simulate the fully drained condition, the constitutive equation can be obtained by combining Equations (A-7), (A-8), and (A-9) as

$$\dot{\boldsymbol{\sigma}}=\boldsymbol{D}^{\mathrm{net}}:\dot{\boldsymbol{\varepsilon}} \tag{A-19}$$

where $\boldsymbol{D}^{\mathrm{net}}$ is given by Equation (A-5).

Constitutive relationship for exhausted air and undrained water condition (constant water content condition)

The constant water content condition, that is, exhausted air and undrained water, is the condition that air is able to drain out of the soil but water is unable to do so. So as to simulate the constant water content condition, the constitutive equations can be obtained by combining Equations (A-7), (A-8), and (A-18) as

$$\begin{cases}\dot{\boldsymbol{\sigma}}=\boldsymbol{D}^{\mathrm{net}}:\dot{\boldsymbol{\varepsilon}}+\boldsymbol{D}^{\mathrm{s}}\dot{u_{\mathrm{w}}}\\ 0=\left[\left(1-\dfrac{\partial S_{\mathrm{r}}\mathrm{d}I_{\mathrm{h}}}{\partial I_{\mathrm{h}}\mathrm{d}S_{\mathrm{r}}}\right)\left(\dfrac{S_{\mathrm{r}}}{e}\right)+\dfrac{\partial S_{\mathrm{r}}}{\partial e}\right]v_0\mathbf{1}:\dot{\boldsymbol{\varepsilon}}+\dfrac{\partial S_{\mathrm{r}}}{\partial s}\dot{u_{\mathrm{w}}}\end{cases} \tag{A-20}$$

Constitutive equations for unexhausted air and undrained water condition (fully undrained condition)

The fully undrained condition, that is, unexhausted air and undrained water, is the condition that air and water are unable to drain out of the soil. In other words, the masses of water and air are constant. So as to simulate the fully undrained condition, we first subtract Equations (A-14) from (A-18):

$$0=\left[\left(1-\frac{\partial S_{\mathrm{r}}\mathrm{d}I_{\mathrm{h}}}{\partial I_{\mathrm{h}}\mathrm{d}S_{\mathrm{r}}}\right)\frac{1}{e}\right]v_0\mathbf{1}:\dot{\boldsymbol{\varepsilon}}-\left[\left(1-\frac{\partial S_{\mathrm{r}}\mathrm{d}I_{\mathrm{h}}}{\partial I_{\mathrm{h}}\mathrm{d}S_{\mathrm{r}}}\right)\frac{(1-S_{\mathrm{r}})}{u_{\mathrm{a}}}\right]\dot{u_{\mathrm{a}}} \tag{A-21}$$

Combining Equations (A-4), (A-18), and (A-21), the constitutive equations for the fully undrained condition can be obtained as

DOI: 10.1002/nag

$$\begin{cases} \dot{\boldsymbol{\sigma}} = \boldsymbol{D}^{\text{net}} : \dot{\boldsymbol{\varepsilon}} + (\mathbf{1} - \boldsymbol{D}^{\text{s}})\dot{u_{\text{a}}} + \boldsymbol{D}^{\text{s}}\dot{u_{\text{w}}} \\ 0 = \left[\left(1 - \dfrac{\partial S_{\text{r}} \mathrm{d}I_{\text{h}}}{\partial I_{\text{h}} \mathrm{d}S_{\text{r}}}\right)\dfrac{1}{e}\right] v_0 \mathbf{1} : \dot{\boldsymbol{\varepsilon}} - \left[\left(1 - \dfrac{\partial S_{\text{r}} \mathrm{d}I_{\text{h}}}{\partial I_{\text{h}} \mathrm{d}S_{\text{r}}}\right)\dfrac{(1 - S_{\text{r}})}{u_{\text{a}}}\right]\dot{u_{\text{a}}} \\ 0 = \left[\left(1 - \dfrac{\partial S_{\text{r}} \mathrm{d}I_{\text{w}}}{\partial I_{\text{w}} \mathrm{d}S_{\text{r}}}\right)\left(\dfrac{S_{\text{r}}}{e}\right) + \dfrac{\partial S_{\text{r}}}{\partial e}\right] v_0 \mathbf{1} : \dot{\boldsymbol{\varepsilon}} - \dfrac{\partial S_{\text{r}}}{\partial s}\dot{u_{\text{a}}} + \dfrac{\partial S_{\text{r}}}{\partial s}\dot{u_{\text{w}}} \end{cases} \tag{A-22}$$

ACKNOWLEDGEMENTS

The first author would like to express his gratitude to MEXT for granting him the Monbukagakusho Scholarship. This work was funded by JSPS KAKENHI under grants 24360192 and 16H06099 to the corresponding author. The corresponding author also wishes to acknowledge the generous support provided by the Nippon Expressway group of companies through their funds for disaster prevention measures for expressways. Finally, the authors would like to extend their gratitude to Dr Unno (Associate Professor, Utsunomiya University) for providing the experimental data on Tsukidate soil.

REFERENCES

1. Unno T, Kazama M, Sento N, Uzuoka R. Cyclic shear behavior of unsaturated volcanic sandy soil under various suction conditions. *Proceedings of the 4th International Conference on Unsaturated Soils*, Arizona, 2006; 1133–1144.
2. Konagai K, Kiyota T, Suyama S, Asakura T, Shibuya K, Eto C. Maps of soil subsidence for Tokyo bay shore areas liquefied in the March 11th, 2011 off the Pacific Coast of Tohoku Earthquake. *Soil Dynamics and Earthquake Engineering* 2013; **53**:240–253.
3. Ishihara K, Tsukamoto Y, Kamada K. Undrained behaviour of near-saturated sand in cyclic and monotonic loading. In *Proceedings of the International Conference on Cyclic Behavior of Soils and Liquefaction Phenomena*, Triantafyllidis T (ed.): Bochum, 2004; 27–39.
4. Selim AA, Burak G. Cyclic stress–strain behavior of partially saturated soils. *Proceedings of the 4th International Conference on Unsaturated Soils*, Arizona, 2006; 497–507.
5. Okamura M, Noguchi K. Liquefaction resistances of unsaturated non-plastic silt. *Soils and Foundations* 2009; **49**(2):221–229.
6. Liu C, Xu J. Experimental study on effects of initial conditions on liquefaction of saturated and unsaturated sand. *International Journal of Geomechanics* 2013:15(6).
7. Tsukamoto Y, Kawabe S, Matsumoto J, Hagiwara S. Cyclic resistance of two unsaturated silty sands against soil liquefaction. *Soils and Foundations* 2014; **54**(6):1094–1103.
8. Unno T, Kazama M, Uzuoka R, Sento N. Liquefaction of unsaturated sand considering the pore air pressure and volume compressibility of the soil particle skeleton. *Soils and Foundations* 2008; **48**(1):87–99.
9. Unno T, Uzuoka R, Sento N, Kazama M. Pore air pressure effect on cyclic shear behavior of undrained sandy soil. *Journal of Japan Society of Civil Engineers* 2013; **69**(3):386–403.
10. Khalili N, Habte MA, Zargarbashi S. A fully coupled flow deformation model for cyclic analysis of unsaturated soils including hydraulic and mechanical hystereses. *Computers and Geotechnics* 2008; **35**(6):872–889.
11. Yang C, Cui YJ, Pereira JM, Huang MS. A constitutive model for unsaturated cemented soils under cyclic loading. *Computers and Geotechnics* 2008; **35**(6):853–859.
12. Kikumoto M, Kyokawa H, Nakai T, Shahin HM. A simple elasto–plastic model for unsaturated soils and interpretations of collapse and compaction behaviours. In *Proceedings of the 5th International Conference on Unsaturated Soils*, Alonso E, Gens A (eds.): Barcelona, 2010; 849–855.
13. Liu C, Muraleetharan KK. Coupled hydro-mechanical elastoplastic constitutive model for unsaturated sands and silts. *I: Formulation. International Journal of Geomechanics* 2012a; **12**(3):239–247.
14. Liu C, Muraleetharan KK. Coupled hydro-mechanical elastoplastic constitutive model for unsaturated sands and silts. II: integration, calibration, and validation. *International Journal of Geomechanics* 2012b; **12**(3):248–259.
15. Hashiguchi K, Ueno M. Elastoplastic constitutive laws of granular material. In *Proceedings of the 9th International Conference on Soil Mechanics and Foundation Engineering*, Murayama S, Schofield AN (eds.): Tokyo, 1977; 73–82.
16. Sivakumar V. A critical state framework for unsaturated soil. *Ph.D. Thesis*, University of Sheffield, 1993.
17. Bishop AW. The principal of effective stress. *Teknisk Ukeblad* 1959; **106**(39):859–863.
18. Schrefler BA. The finite element method in soil consolidation (with applications to surface subsidence), *Ph.D. Thesis*, University College of Swansea, 1984.
19. Borja RI. On the mechanical energy and effective stress in saturated and unsaturated continua. *International Journal of Solids and Structures* 2006; **43**:1764–1786.
20. Gardner WR. Some steady state solutions of the unsaturated moisture flow equation with application to evaporation from a water table. *Soil Science* 1958; **85**(4):228–232.
21. Brooks RH, Corey AT. *Hydraulic Properties of Porous Media, Hydrology Paper 3*. Colorado State University: Fort Collins, 1964.

DOI: 10.1002/nag

22. Fredlund DG, Xing A. Equation for the soil–water characteristic curve. *Canadian Geotechnical Journal* 1994; **31**(3):521–532.
23. van Genuchten MT. A closed form equation for predicting the hydraulic conductivity of unsaturated soil. *Soil Science Society of America Journal* 1980; **44**:892–898.
24. Tarantino A, Tombolato S. Coupling of hydraulic and mechanical behaviour in unsaturated compacted clay. *Geotechnique* 2005; **55**(4):307–317.
25. Hains WB. Studies in the physical properties of soil: 5, The hysteresis effect in capillary properties, and the modes of moisture distribution associated therewith. *The Journal of Agricultural Science* 1939; **20**:97–116.
26. Topp GC, Miller EE. Hysteretic moisture characteristics and hydraulic conductivities for grass–bead media. *Soil Science Society of America Journal* 1966; **30**:156–162.
27. Huang HC, Tan YC, Liu CW, Chen CH. A novel hysteresis model in unsaturated soils. *Hydrological Process* 2005; **19**(8):1653–1665.
28. Roscoe KH, Burland JB. On the generalised stress–strain behaviour of "wet" clay. In *Engineering Plasticity*, Heyman J, Leckie FA (eds.). Cambridge University Press, 1968; 535–609.
29. Been K, Jefferies M. A state parameter for sands. *Geotechnique* 1985; **35**(2):99–112.
30. Okamura M, Soga Y. Effects of pore fluid compressibility on liquefaction resistance of partially saturated sand. *Soils and Foundations* 2006; **46**(5):695–700.
31. Kazama M, Yamaguchi A, Yanagisawa E. Liquefaction resistance from a ductility viewpoint. *Soils and Foundations* 2000; **40**(6):47–60.

DOI: 10.1002/nag